DIFFRACTIVE DIJET ANALYSIS

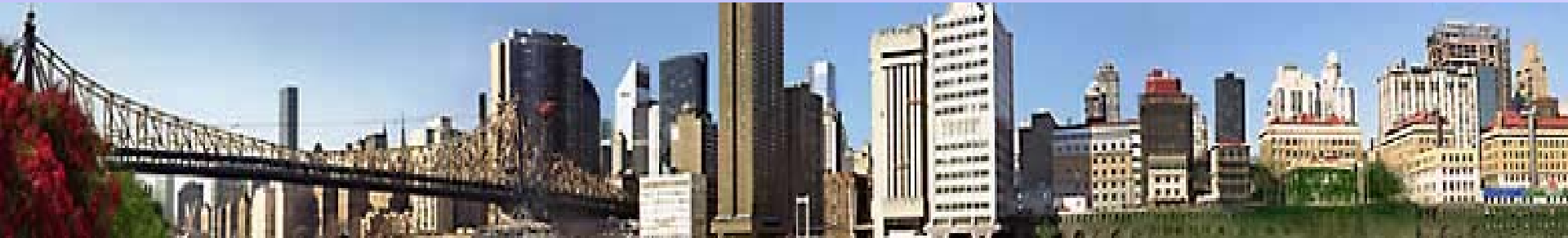
➔ FULL UPDATE ←

QCD group, 8/26/2010

Primary authors: Michele Gallinaro and Dino Goulianos
GPs: Giorgio Bellettini and Mario Martinez Perez

documentation: CDF 7832 and CDF 7877
http://www-cdf.fnal.gov/internal/physics/godparents/diff_dijets/

first draft submitted to GPs: August 4, 2006 (see webpage)
update: August 4,2006 (see webpage) – also more recently?
update talk to GPs: August 8, 2006



Contents

- ✓ Introduction
- ✓ Presentation of paper draft
  - ❖ what remains to be blessed
- ✓ Discussion

p-p Interactions

Non-diffractive:

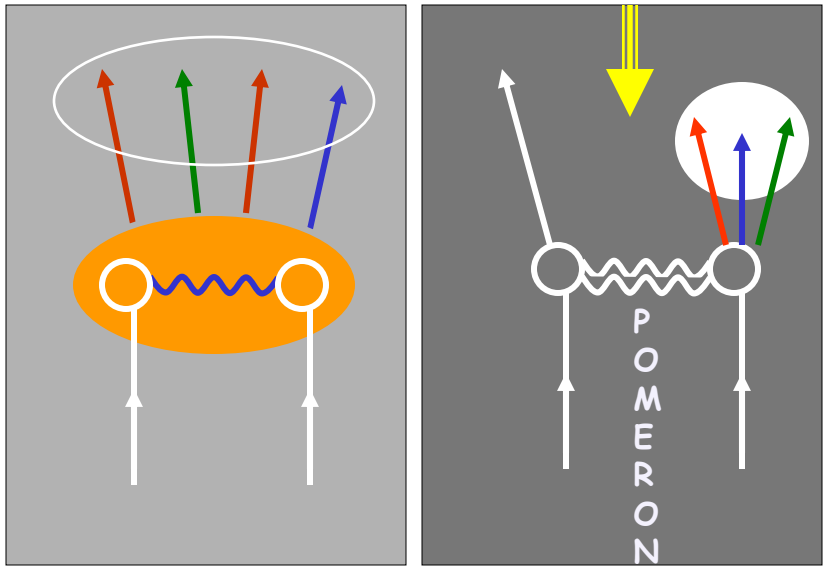
Color-exchange

Diffractive:

Colorless exchange carrying vacuum quantum numbers

rapidity gap

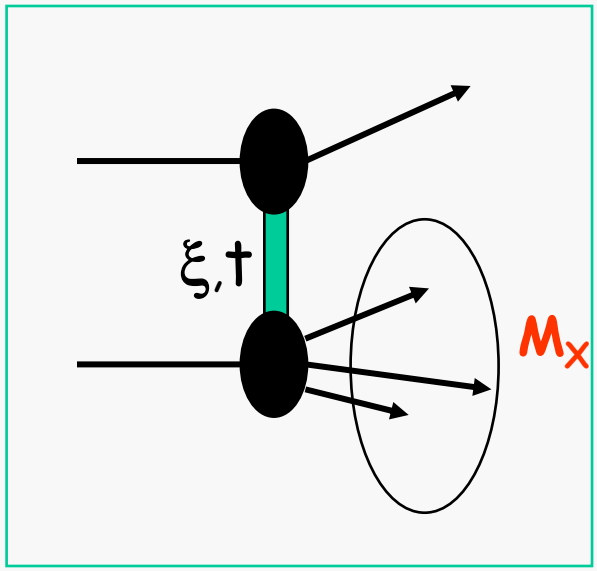
Incident hadrons acquire color and break apart

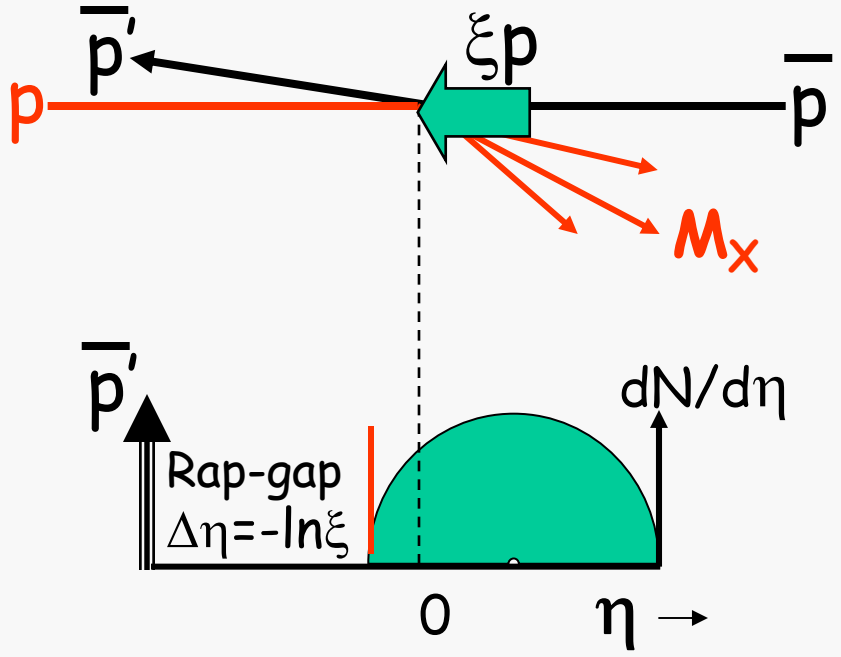


Incident hadrons retain their quantum numbers remaining colorless

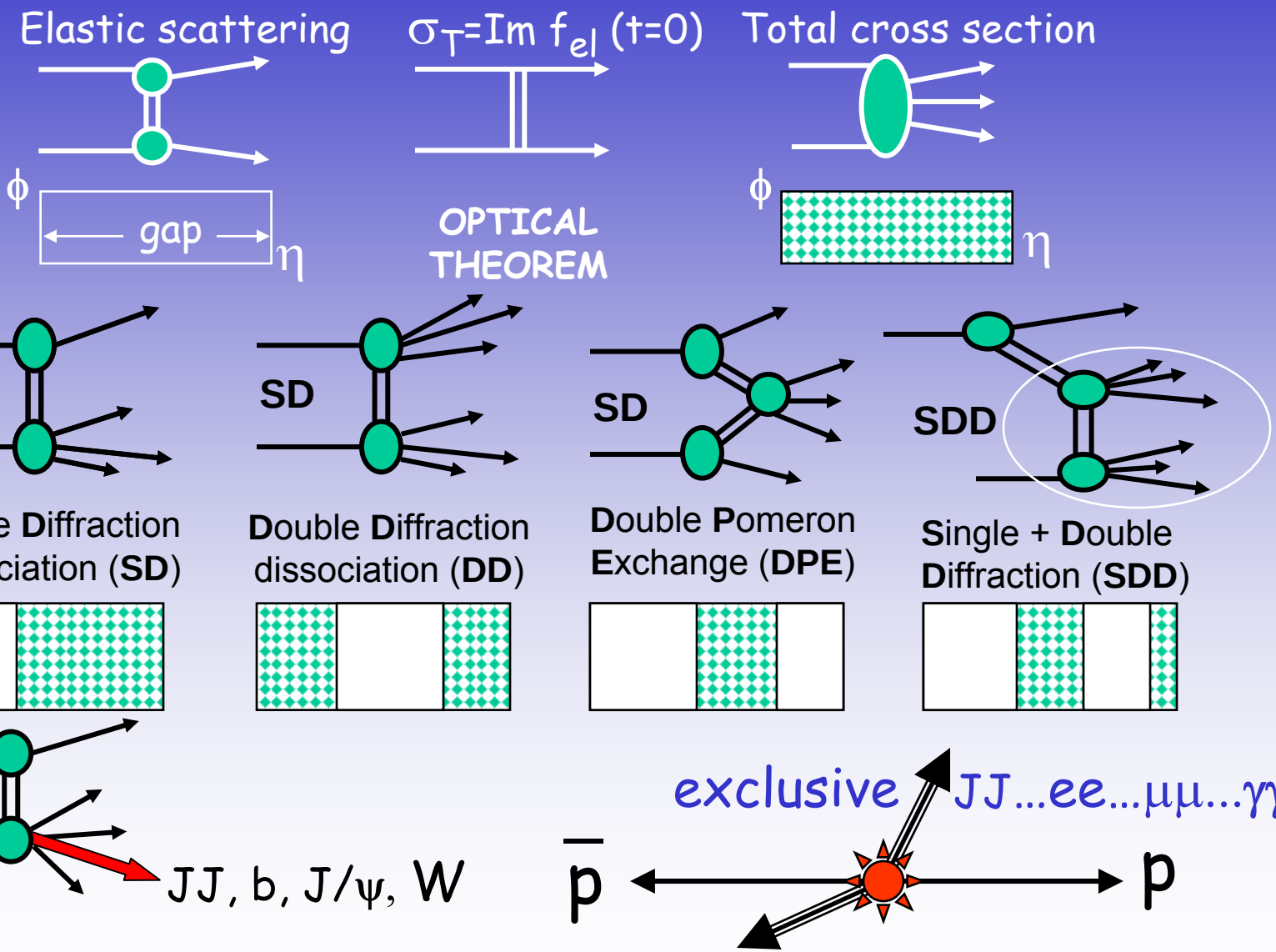
Goal: understand the QCD nature of the diffractive exchange

Definitions



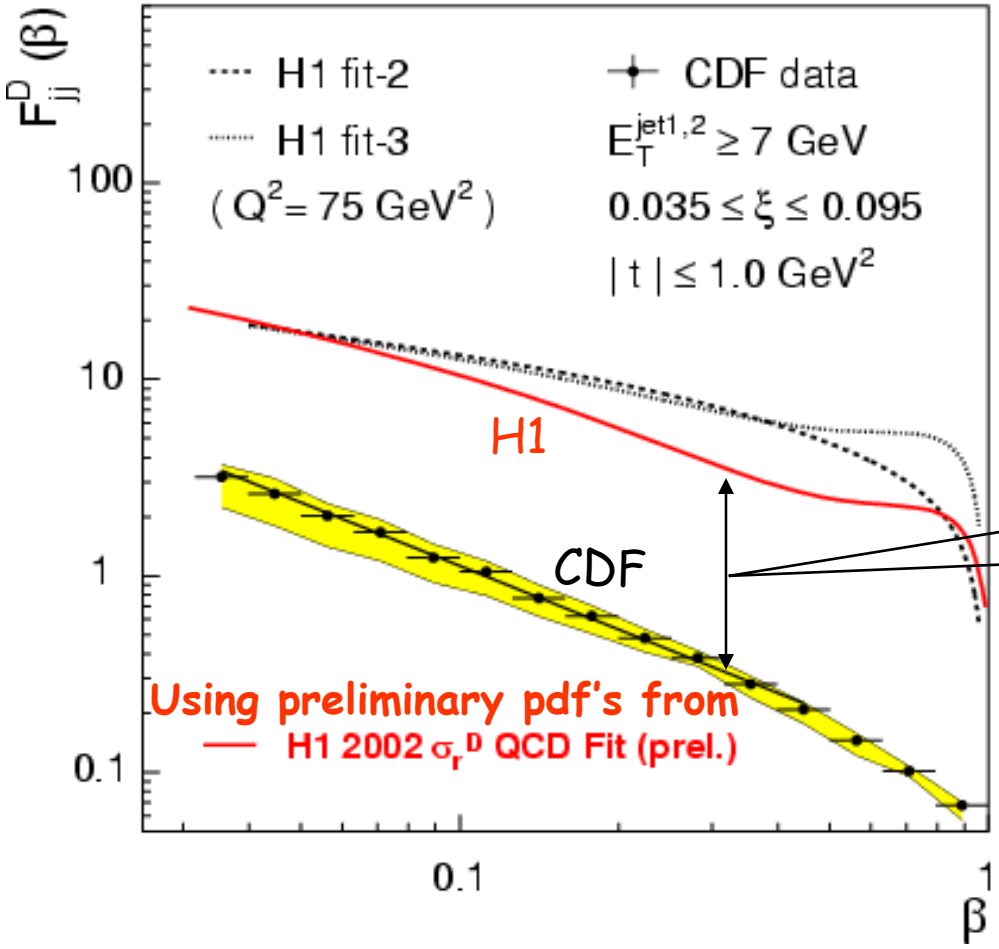


Diffraction at CDF



Run I - Diffractive Structure Function (DSF)

Breakdown of QCD factorization



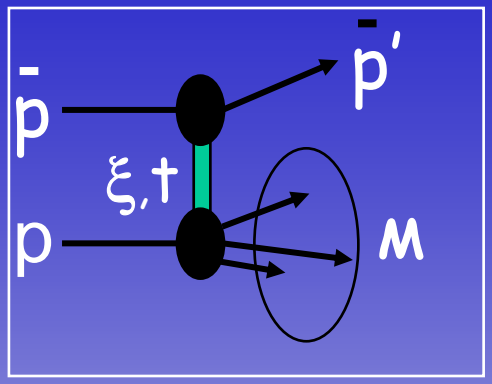
$$\bar{p}p \rightarrow \bar{p} + \text{dijet} + X$$

same suppression
as in soft diffraction

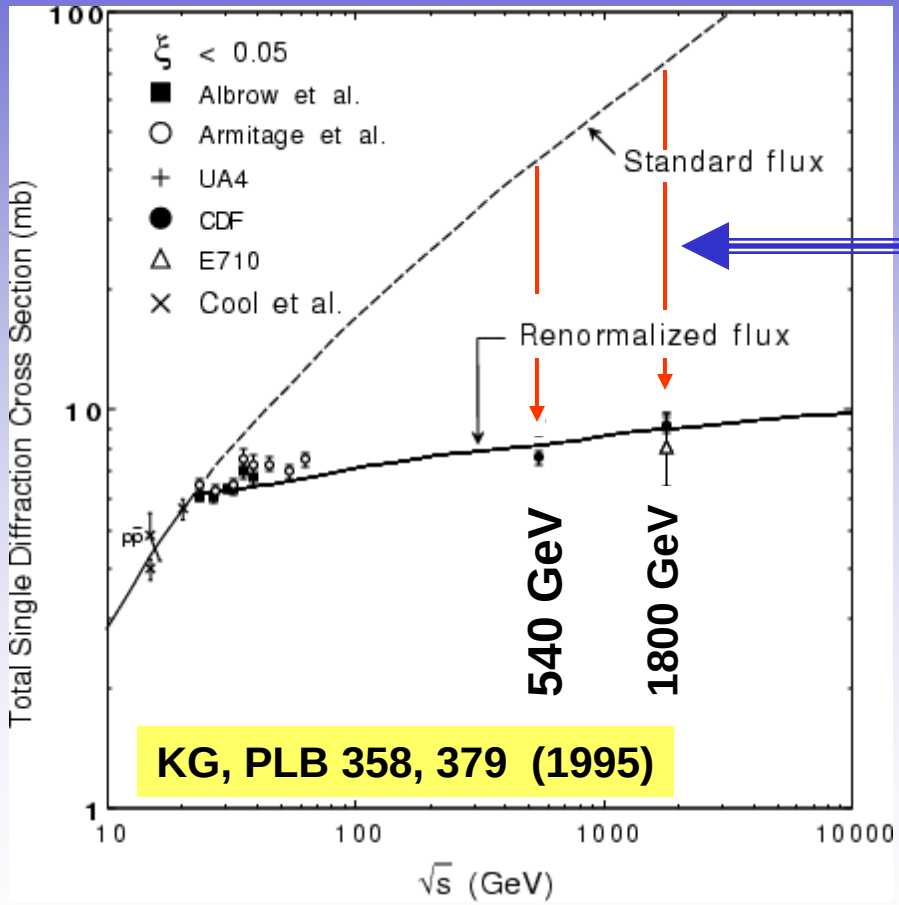
momentum fraction
of parton in Pomeron

σ^{T}_{SD} (pp & $\bar{p}p$)

➔ suppressed relative to Regge prediction



σ^{T}_{SD} mb



Factor of ~8 (~5) suppression at $\sqrt{s}$ = 1800 (540) GeV

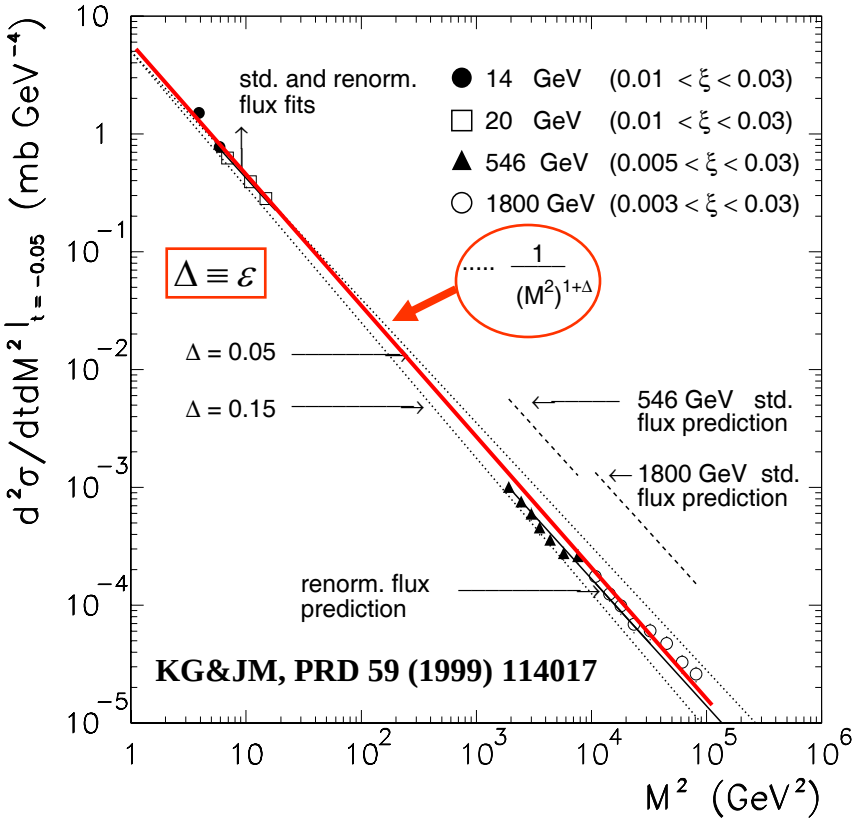
M^2 scaling

➔ $d\sigma/dM^2$ independent of s over 6 orders of magnitude!

renormalization

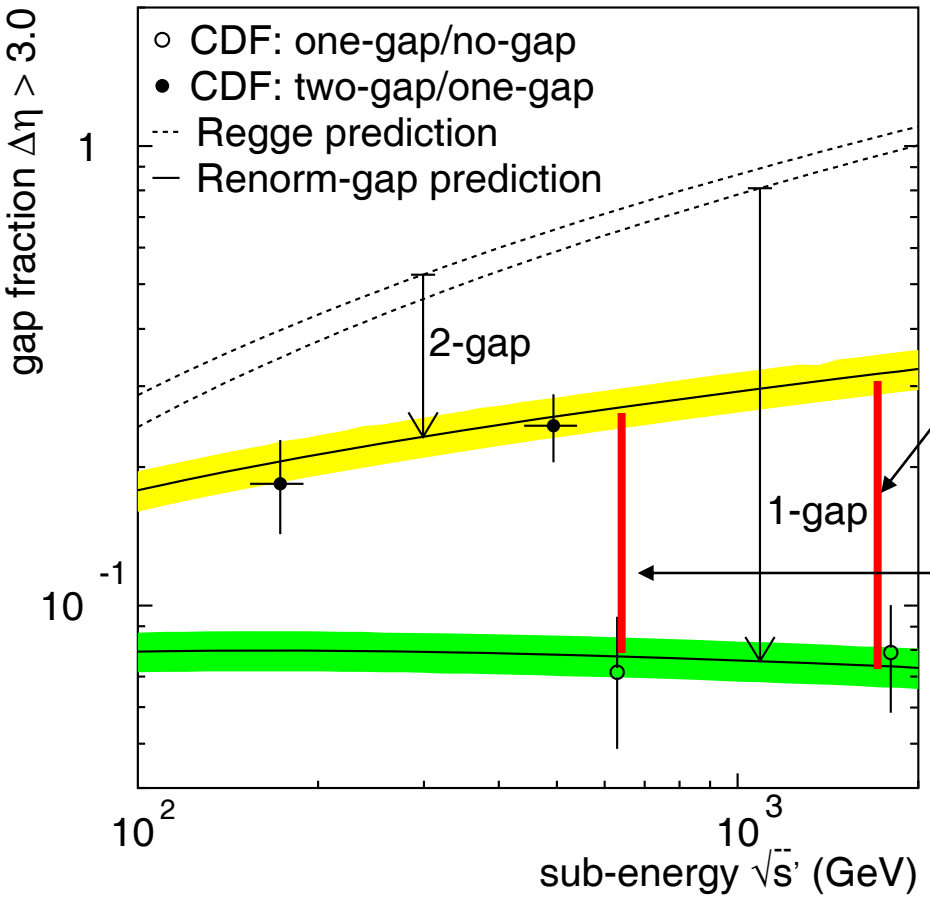
$$\frac{d\sigma}{dM^2} \propto \frac{s^{2\varepsilon} \to 1}{(M^2)^{1+\varepsilon}}$$

➔ Independent of s over 6 orders of magnitude in M^2 !



➔ factorization breaks down to ensure M^2 scaling!

Gap survival probability - S

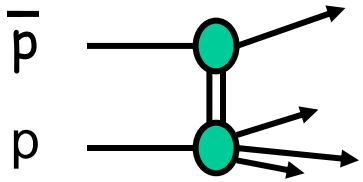


$$S = \frac{\left(\phi \text{ gap}\right)_\eta \,/\, \left(\phi \text{ no gap}\right)_\eta}{\left(\phi \text{ gap}\right)_\eta \,/\, \left(\phi \text{ no gap}\right)_\eta}$$

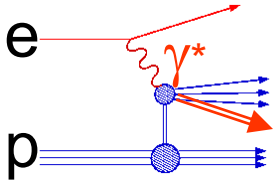
$$S^{1-gap/0-gap}_{2-gap/1-gap}(1800\ \text{GeV}) \approx 0.23$$

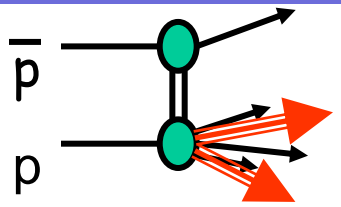
$$S^{1-gap/0-gap}_{2-gap/1-gap}(630\ \text{GeV}) \approx 0.29$$

σ^{T}_{SD} and dijets



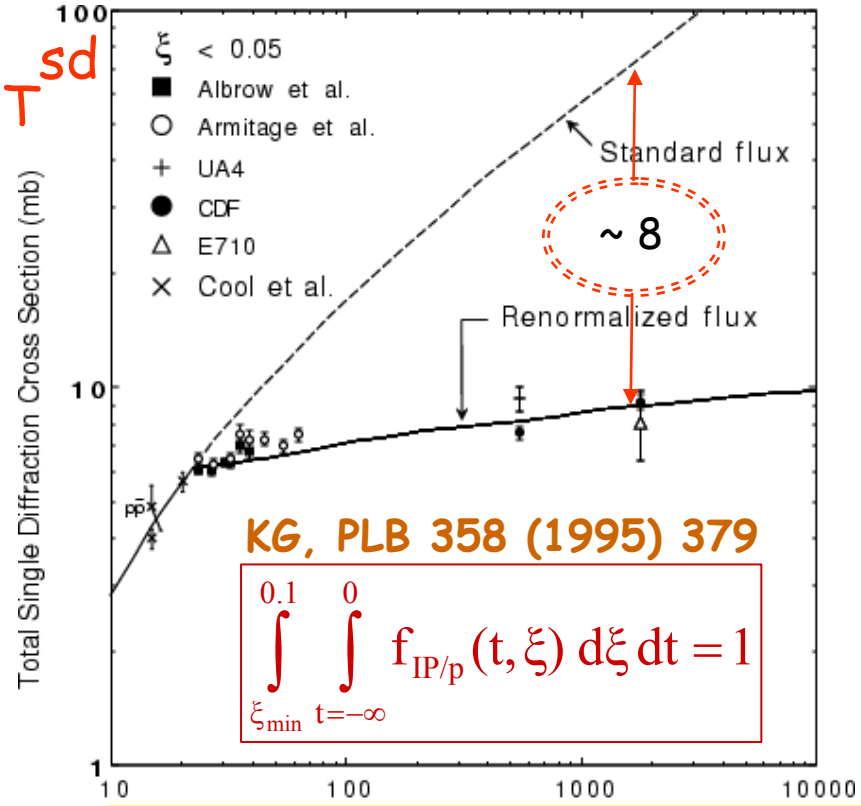
soft

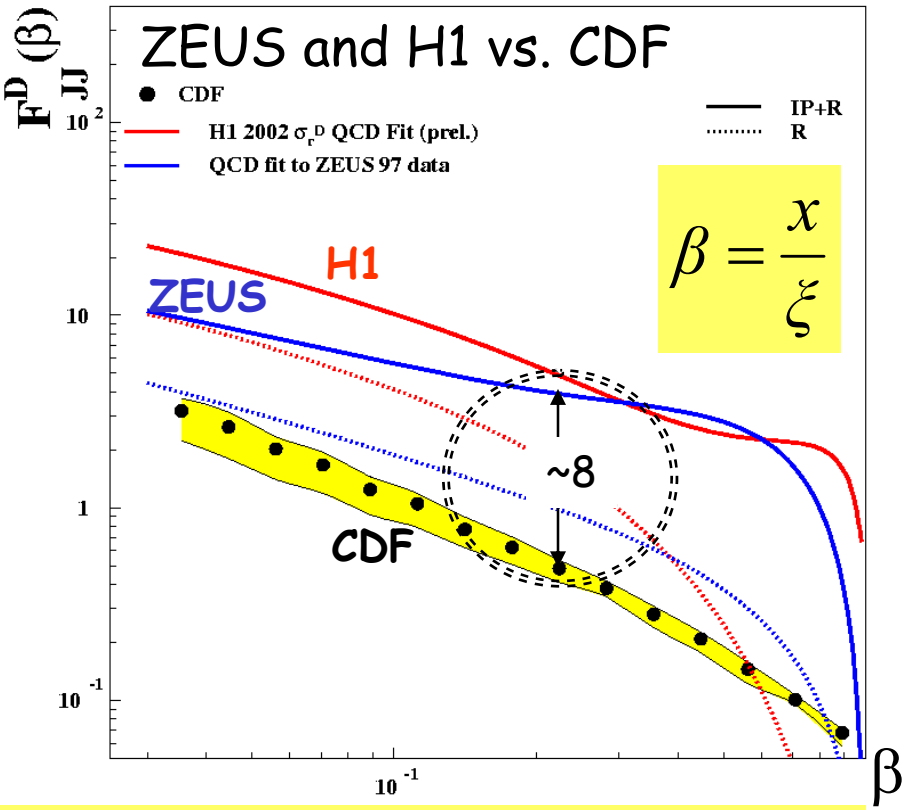




dijet

σ_T^{sd}





Magnitude: same suppression factor in soft and hard diffraction!
Shape of β distribution: ZEUS, H1, and Tevatron – why different slapes?

Diffractive dijet production in $\bar{p}p$ collisions at $\sqrt{s}$=1.96 TeV

M. Gallinaro, K. Goulianos, and K. Terashi
CDF collaboration
(Dated: August 18, 2010)

We report on a study of diffractive dijet production in $p\bar{p}$ collisions at $\sqrt{s}$ = 1.96 TeV using the CDF II detector at the Fermilab Tevatron $p\bar{p}$ collider. A data sample of 310 pb^{-1} collected by triggering on a high transverse energy jet in coincidence with a recoil antiproton detected in a Roman pot spectrometer is used to measure the ratio of single-diffractive to inclusive dijet event rates as a function of the antiproton x-Bjorken ($x^{\bar{p}}_{Bj}$) and $Q^2 \approx (E_T^{jet})^2$ in the range $10^{-3} < x^{\bar{p}}_{Bj} < 0.1$ and $100 < Q^2 < 10^4$ GeV^2, respectively. Results are presented for the region of $\bar{p}$ momentum loss fraction $0.03 < \xi_{\bar{p}} < 0.09$ and a 4-momentum transfer squared $t_{\bar{p}} < -4$ GeV^2. The $t_{\bar{p}}$ dependence is measured as a function of Q^2 and x_{Bj} and compared with that of inclusive single diffraction dissociation. We find a weak $x^{\bar{p}}_{Bj}$ and Q^2 dependence in the ratio of single diffractive to inclusive event rates and no significant Q^2 dependence in the diffractive $|t_{\bar{p}}|$-distributions.

PACS numbers: 13.87.Ce,12.38.Qk,12.40.Na

I. INTRODUCTION

The CDF collaboration has reported several results on soft and hard diffraction obtained at the Fermilab Tevatron $p\bar{p}$ collider [1]-[18], three of which [6, 10, 14] are based on dijet events produced in single diffraction (SD) dissociation:

$$\bar{p} + p \to \bar{p} + gap + [jet_1 + jet_2 + X]. \quad (1)$$

These events are characterized by the presence of two jets in the final state and a leading antiproton which escapes the collision intact. A large forward rapidity gap (region of pseudorapidity [19] devoid of particles) is present between the leading antiproton and the diffractive cluster, defined as the rapidity region in which particles are produced [20]. The result that has received the most attention is the breakdown of QCD factorization expressed as a suppression by a factor of $\sim \mathcal{O}(10)$ of the diffractive structure function (DSF) measured by CDF relative to that derived from fits to parton densities measured in diffractive deep inelastic scattering (DDIS) at the DESY e-p collider HERA (see [10]). This striking result was further explored by CDF in studies of other diffractive processes, as briefly described below. The present measurement aims at further characterizing the properties of diffractive dijet production in an effort to decipher the QCD nature of the diffractive exchange, traditionally referred to as the *Pomeron* [21]-[23].

The CDF diffractive program started with the first Tevatron collider run in 1989, which is known as Run I–0. The program continued through Runs I–A, B, C (1992–1995), was extended through the use of upgraded detectors and new triggers in Run II–A (2003–2006) and Run II–B (2006–), and is now in its final phase of Run II data analysis. Two papers have already been published from Run II data [17, 18].

In Run I, several soft and hard diffraction processes were studied at $\sqrt{s}$ = 1800 GeV and in some cases at $\sqrt{s}$ = 630 GeV. Two types of hard diffraction results were obtained:

(a) gap results: diffractive to non-diffractive (ND) cross section ratios using the rapidity gap signature to select diffractive events;

(b) RPS results: diffractive to ND structure function ratios using a Roman Pot Spectrometer (RPS) to trigger on a leading antiproton.

The diffractive dijet production processes studied are shown schematically in Fig. 1. They include (a) single diffraction (SD), (b) double diffraction (DD), and (c) double Pomeron exchange (DPE) processes. For SD, results have also been obtained for W [5], b-quark [9], and J/ψ [13] production.

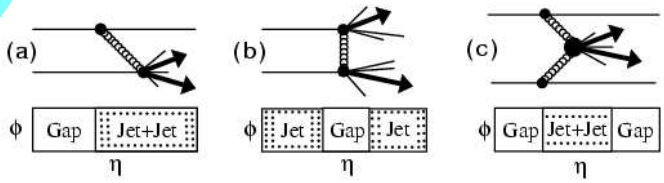


FIG. 1: Leading order schematic diagrams and η-ϕ event topologies for dijet diffractive processes studied by CDF: (a) single diffraction (SD), (b) double diffraction (DD), and (c) double Pomeron exchange (DPE).

Soft diffraction processes studied include SD [3], DD [12], DPE [16], and single plus double diffraction (SDD) [15]. These processes are defined as follows:

SD $\bar{p}p \to \bar{p} + \text{gap} + [p \to X_p]$,
DD $\bar{p}p \to [\bar{p} \to X_{\bar{p}}] + \text{gap} + [p \to X_p]$,
DPE $\bar{p}p \to \bar{p} + \text{gap} + X_c + \text{gap} + p$,
SDD $\bar{p}p \to \bar{p} + \text{gap} + X_c + \text{gap} + [p \to X_p]$,

where X_p (X_c) represent proton (central) dissociation clusters of particles.

DRAFT

The results obtained exhibit regularities in normalization and factorization properties that point to the QCD character of diffraction [24]. For example, at $\sqrt{s}$ =1800 GeV the SD/ND ratios, also referred to as diffractive- or gap-fractions, for dijet, W, b-quark, and J/ψ production, as well the ratio of DD/ND dijet production, are all $\approx 1\%$. This value is suppressed relative to standard QCD-inspired theoretical expectations (*e.g.* 2-gluon exchange) by a factor of $\sim$10, which is comparable to the suppression factor observed in soft diffraction relative to Regge theory based predictions. However, except for an overall suppression in normalization, factorization approximately holds among different processes at fixed $\sqrt{s}$ [24].

In Run II, the main goal of the diffractive program of CDF has been to obtain results which can help decipher the QCD nature of the diffractive exchange. In this paper, we report on the x-Bjorken, Q^2 and t dependence of the diffractive structure function measured from dijet production in association with a leading antiproton in $\bar{p}p$ collisions at $\sqrt{s}$=1.96 TeV and compare our results with results from HERA and with theoretical expectations.

The paper is organized as follows: in Sec. II we discuss the method we use to extract the DSF, in Sec. III we describe the experimental apparatus, in Secs. IV and V we discuss the data sets and data analysis, in Sec. VI we present the results, and in Sec. VII we summarize the results and draw conclusions.

II. METHOD

The cross section for inclusive dijet production in $\bar{p}p$ collisions can be written as

$$\frac{d^3\sigma_{jj}^{incl}}{dx_p dx_{\bar{p}} dt} = \frac{F_{jj}(x_p,Q^2)}{x_p}\cdot\frac{F_{jj}(x_{\bar{p}},Q^2)}{x_{\bar{p}}}\cdot\frac{d\sigma_{jj}}{dt}, \quad (2)$$

where x_p ($x_{\bar{p}}$) is the Bjorken variable representing the momentum fraction of the interacting parton in the proton (antiproton), Q^2 is the momentum transfer squared, $F_{jj}(x_p,Q^2)$ and $F_{jj}(x_{\bar{p}},Q^2)$ are structure functions, σ_{jj} is the scattering cross section of the two partons producing the final-state jets, and t is the square of the four-momentum transfer of the interacting partons.

The structure function relevant for dijet production is a color-weighted combination of gluon (g) and quark (q) terms given by:

$$F_{jj}(x,Q^2) = x\left[g(x,Q^2)+\frac{4}{9}\sum_i q_i(x,Q^2)\right]. \quad (3)$$

In analogy with Eq. (2), the differential cross section for diffractive dijet production can be written as [25]

$$\frac{d^4\sigma_{jj}^{SD}}{dx_p dx_{\bar{p}} d\xi dt} = \frac{F_{jj}(x_p,Q^2)}{x_p}\cdot\frac{F_{jj}^{SD}(x_{\bar{p}},Q^2,\xi,t)}{x_{\bar{p}}}\cdot\frac{d\sigma_{jj}}{dt}, \quad (4)$$

where F_{jj}^{SD} is the DSF, which in addition to the usual dependence on $x_{\bar{p}}$ and Q^2 also depends on ξ, the forward momentum loss of the antiproton [20], and on t.

The jet energies measured in the CDF detector must be corrected for various detector effects, which depend on the jet energy and η-ϕ coordinates due to differences in calorimeter sub-system design and calorimeter interfaces [26]. The correction fraction generally increases as the jet energy decreases. To avoid systematic uncertainties associated with estimating corrections using Monte Carlo simulations, particularly for diffractively produced jets of relatively low E_T, we measure ratios of SD to inclusive production as a function of x-Bjorken and Q^2, for which jet energy corrections due to detector effects cancel out. Below, we will be referring to *inclusive* and *non-diffractive* (ND) dijet production interchangeably as the cross section for diffractive dijet production is $\lessapprox 1\%$ of the cross section for inclusive dijet production.

The DSF is obtained by multiplying the ratio $R_{SD/ND}(x,\xi,t)$ of the SD to ND event densities $n_{jj}^{SD(x,Q^2,\xi,t)}$ and $n_{jj}(x,Q^2)$ by the ND structure function $F_{jj}(x,Q^2)$:

$$F_{jj}^{SD}(x,Q^2,\xi,t) = R_{SD/ND}(x,\xi,t)\times F_{jj}(x,Q^2). \quad (5)$$

This method of measuring diffractive structure functions relies on the LO QCD expectation that cross sections are proportional to structure functions:

$$R_{SD/ND}(x,\xi,t) = \frac{n_{jj}^{SD}(x,Q^2,\xi,t)}{n_{jj}(x,Q^2)} \approx \frac{F_{jj}^{SD}(x,Q^2,\xi,t)}{F_{jj}(x,Q^2)}. \quad (6)$$

Next to leading order corrections to $F_{jj}^{SD}(x,Q^2,\xi,t)$ obtained by this method are expected to be of $\mathcal{O}(10)$ % [27].

III. EXPERIMENTAL APPARATUS

The CDF II detector was equipped with special forward detectors [18, 28–30] designed to enhance the capabilities for studies of diffractive physics. These detectors included the *RPS*, the *Beam Shower Counters* (BSC), and the *MiniPlug* (MP) calorimeters. The RPS is a scintillator fiber tracker used to detect leading antiprotons; the BSC are scintillator counters installed around the beam-pipe at three (four) locations along the p ($\bar{p}$) direction and are used to identify rapidity gaps in the region $5.5 < |\eta| < 7.5$; and the MP calorimeters [29] are two lead-scinillator based forward calorimeters [29] covering the pseudorapidity region $3.6 < |\eta| < 5.1$. The forward detectors included a system of Cherenkov luminosity counters (CLC) [31], whose primary function was to measure the number of inelastic $\bar{p}p$ collisions per beam-bunch crossing and thereby the luminosity. The CLC covered the range $3.7 < |\eta| < 4.7$, which substantially

DRAFT

overlaps the MP coverage. In this analysis, they were used for diagnostic purposes to refine the rapidity gap definition by detecting charged particles that might penetrate a MP without interacting and yield a pulse-height smaller than the MP tower thresholds and be undetected.

Figure 2 shows a schematic side view of the beam-line elements and forward detectors along the outgoing antiproton beam direction. The CLC, which was located iside the toroid, is not shown. The RPS comprises three Roman pot stations located at a distance of ~ 57 m from the nominal interaction point (IP) along the outgoing $\bar{p}$ direction. Each station is equipped with one Roman Pot Trigger (RPT) counter and an 80-channel scintillator-fiber tracker, which can be used to reconstruct tracks both in the X (horizontal) and Y (vertical)coordinates. The tracking information in conjunction with the IP coordinates provided by the central detector can be used to calculate the variables ξ and t of the recoil antiproton. During running, the RPS detectors were brought up to a distance of $X \approx 1$ cm from the outgoing antiproton beam, with the incoming proton beam positioned ~ 2 mm further away. In Run I, in which data were taken at lower luminosities, the RPS detectors were positioned at approximately the same distance from the antiproton beam, but the more intense proton beam was in-between the antiproton beam and the detectors. Reversing the polarity of the accelerator electrostatic beam separators brought the antiproton beam on the RPS side and enabled running with the detectors at the same distance from the antiproton beam at the higher luminosities of Run II.

The CDF I and CDF II main detectors are multipurpose detectors described in detail in Refs. [32, 33]. The most relevant components of CDF II for this analysis are the charged particle tracking system and the central and plug calorimeters. The tracking system consists of a silicon vertex detector surrounded by the Central Outer Tracker (COT) [35]. The part of the silicon vertex tetecor used is the SVX II [34], composed of double-sided microstrip silicon sensors arranged in five cylindrical shells of radii between 2.5 and 10.6 cm. The COT is an open-cell drift chamber consisting of 96 layers organized in 8 superlayers with alternating structures of axial and $\pm 2^\circ$ stereo readout within a radial range between 40 and 137 cm. Surrounding the tracking detectors is a superconducting solenoid, which provides a magnetic field of 1.4 T. Calorimeters located outside the solenoid are physically divided into a central calorimeter (CCAL) [36, 37], covering the pseudorapidity range $|\eta| < 1.1$, and a plug calorimeter (PCAL) [38], covering the region $1.1 < |\eta| < 3.6$. These calorimeters are segmented into projective towers of granularity $\Delta\eta \times \Delta\phi \approx 0.1 \times 15^\circ$.

IV. DATA SAMPLES AND EVENT SELECTION

The Run I diffractive dijet results were obtained from diffractive data samples collected al low instantaneous luminosities to avoid background from overlapping events. Constrained by statistics, the Q^2 dependence of the DSF was measured over a limited range. Moreover, due to uncertainties in the beam position at the RPS location, it was difficult to reliably extract normalized t-distributions. In Run II, our goal was to obtain high statistics diffractive data samples with low overlap backgrounds from which to extract the Q^2 and t dependence over a wide range. To achieve this goal, we built special forward detectors, described above in Sec. III, implemented dedicated triggers, and developed analysis techniques for background subtraction and RPS alignment. In this section, we present the data samples and event selection requirements applied to produce the data sets from which the results were extracted.

This analysis is based on data from an integrated luminosity $\mathcal{L} \approx 128$ pb^{-1} collected in 2002–2003. Only "good runs" with a minimum $\mathcal{L} \approx 10$ nb^{-1} are used, selected based on beam conditions, detector performance criteria, and the requirement that the following detector components be functional: CCAL, PCAL, MP, CLC, and BSC. Dedicated level 1, 2, and 3 triggers (L1, L2, and L3) accepted soft interaction events as well as hard interaction events containing high E_T jets. The latter were selected at the trigger level by requiring at least one calorimeter tower with $E_T > 5$, 20, or 50 GeV within $|\eta| < 3.5$. Leading antiprotons with fractional momentum loss in the range $0.03 \lesssim \xi_{\bar{p}} \lesssim 0.09$ were detected using a three-fold coincidence of the RPT counters.

Jets were reconstructed using a cone algorithm, in which the transverse energy of a jet is defined as $E_T^{jet} \equiv \Sigma_i E_i \sin(\theta_i)$ with the sum carried over all calorimeter towers at polar angles θ_i within the jet cone. The midpoint algorithm [40] was used, which is an improved iterative cone clustering algorithm based on calorimeter towers with $E_T > 100$ MeV. The jets were corrected for detector effects and for contributions from the underlying event (UE) [26]. Dijet candidate events were required to have at least two jets with $E_T > 5$, 20, or 50 GeV depending on the event sample, and $|\eta| < 2.5$.

In order to explore the region of large transverse energy jets of relatively low cross sections, data samples of RPS triggered events in conjunction with the presence of a jet with $E_T^{jet} \geq 5$, 20, or 50 GeV in CCAL or PCAL were also studied. These samples are referred to as RPS·Jet5, RPS·Jet20, and RPS·Jet50. Corresponding ND samples (Jet5, Jet20, and Jet50) were used for comparison.

The majority of the data used in this analysis were recorded without tracking information. For these data, the value of ξ was evaluated from calorimeter information and will be referred to as $\xi_{\bar{p}}^{CAL}$ (see Sec. V C). The $\xi_{\bar{p}}^{CAL}$ was then calibrated against ξ obtained from the RPS, $\xi_{\bar{p}}^{RPS}$, using data from runs in which RPS tracking was available (see Sec. V E). Below we list the definitions of

DRAFT

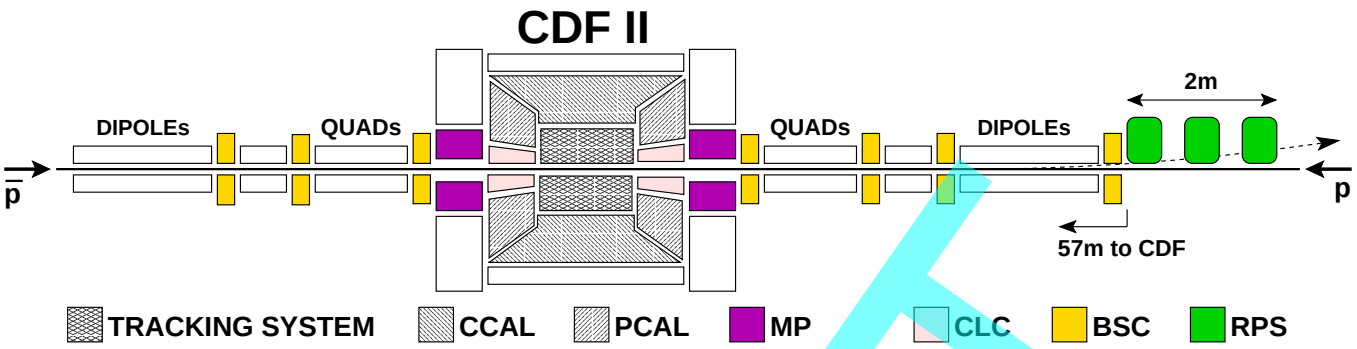


FIG. 2: Schematic layout of the CDF II central and forward detectors.

the triggers used in data acquisition and the data selection requirements applied in obtaining the data samples for this analysis.

The following trigger definitions are used:

- RPS: triple coincidence among the three RPS trigger counters in time with a $\bar{p}$ gate;
- $\text{RPS}_{\text{track}}$: RPS with RPS tracking available (included in the RPS trigger);
- J5, J20, J50: jet with $E_T^{jet} \geq 5$, 20, 50 GeV in CCAL or PCAL;
- RPS·Jet5 (Jet20, Jet50): RPS in coincide with J5, J20, J50.

The data selection requirements are listed below:

(i) good-run events: accepts events from runs with no problems caused by hardware or software failures during data acquisition;

(ii) $\not\!\!E_T$ significance: selects events with missing transverse energy significance $S < 2$ to reject jet events in which there is $\not\!\!E_T$ due to energy loss in calorimeter cracks and/or events with jets and (undetected) neutrinos, such as from $W \to l\nu + jets$ [41];

(iii) $N(jet) \geq 2$: accepts events with two jets of $E_T^{jet} > 5$ GeV within $|\eta^{jet}| < 2.5$;

(iv) splash veto: rejects events that cause splashes (large number of hits) in the RPT counters;

(v) RPT: rejects events that could be triggered by accidental coincidences (less than 0.1%);

(vi) SD ($0.03 < \xi_{\bar{p}}^{CAL} < 0.09$): accepts SD events with good efficiency while rejecting backgrounds from overlapping soft SD events that trigger the RPS and ND dijet event.

Table I lists the number of events surviving these requirements when applied successively to the data.

a. Splash veto The splash events were studied using the $\text{SD}\oplus\text{RPS}_{\text{track}}$ data sample before applying the splash veto requirememnt. The sum of the ADC counts of the three RPT counters, $\text{SumRPT} \equiv \Sigma_{i=1}^{3}\text{RPT}_i^{\text{ADC}}$, is used to reject splash events. Figure 3(a) shows SumRPT for events with/without a reconstructed RPS track. In the "RPS track" histogram the peak at $\sim 3\,000$ ADC counts is attributed to a single MIP traversing all three RPT counters. Two–MIP and three–MIP peaks are also discernible at ~ 6000 and ~ 9000 ADC counts, respectively. Events labeled as "No RPS track" are the splash events. These events dominate the region of SumRPT > 5000. Detailed studies using different event samples indicate that splash events are likely to be due to high $\xi_{\bar{p}}$ diffractive events for which the $\bar{p}$ does not reach the RPS but rather interacts with the material of the beam pipe in the vicinity of the RPS producing a spray of particles causing the splash. In the region of SumRPT < 5000, the "No RPS track" distribution has a peak similar to that seen in the events with a reconstructed RPS track. These events are interpreted as good events for which the track was not reconstructed due to either malfunction or inefficiency of the fiber tracker.

Events with SumRPT> 5000 are rejected. The retained events contain approximately 77 % of the RPT sample, as can be qualitatively seen in Fig. 3(b). These events, after applying the RPT selection requirement, constitute the SD event samples listed in Table I. Any possible inefficiency caused by the SumRPT cut is taken into account by folding a 6 % uncertainty into that of the extracted cross section (see Sec. VI B 1, Table III).

V. DATA ANALYSIS

In this section we discuss analysis details in the following sub-sections:

A – RPS dynamic alignment
B – RPS trigger efficiency
C – Antiprotom momentum loss measurement
D – Multiple interactions
E – Calibration of $\xi_{\bar{p}}^{\text{CAL}}$

DRAFT

TABLE I: Events of data samples surviving successivee selection requirements.

Selection requirement	RPS	RPS·Jet5	RPS·Jet20	RPS·Jet50
Trigger	1 634 723	1 124 243	1 693 644	757 731
good-run events	1 431 460	955 006	1 421 350	561 878
$\not\!\!E_T$ significance: $S_{\not\!\!E} \equiv \not\!\!E_T/\sqrt{\Sigma E_T^2} < 2$	1 431 253	950 776	1 410 780	539 957
$N(jet) \geq 2$: $E_T^{1,2} > 5$ GeV, $\lvert\eta^{1,2}\rvert < 2.5$	59 157	557 615	1 168 881	521 645
splash veto	27 686	259 186	541 031	215 975
RPT	27 680	259 169	541 003	215 974
SD ($0.03 < \xi_{\bar{p}}^{CAL} < 0.09$)	1 458	20 602	26 559	4 432

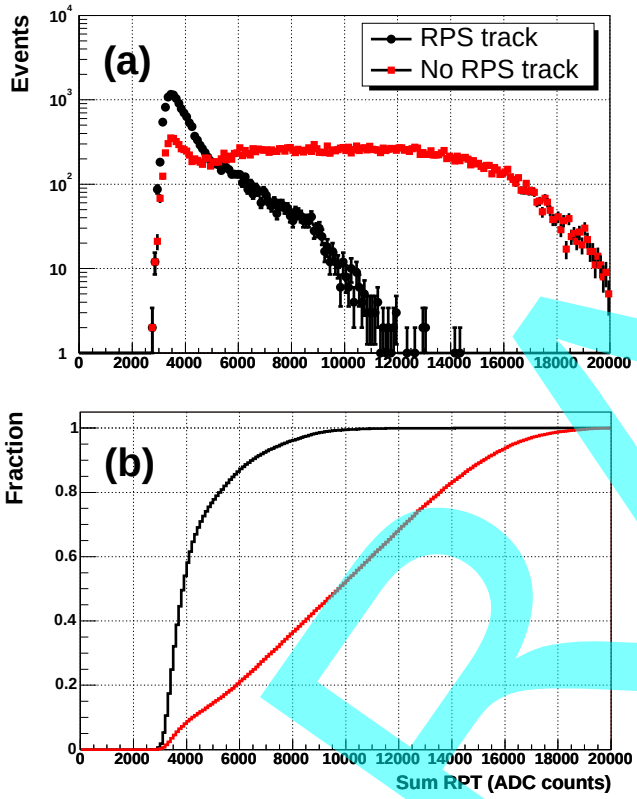


FIG. 3: SumRPT distributions for events of the SD⊕RPS$_{\rm track}$ data sample. (a) Number of events and (b) fraction of events as a function of the sum of ADC counts of the three Roman Pot Trigger (RPT) counters, SumRPT. In (a), the peak at SumRPT$\sim$ 3 000, attributed to a MIP signal, is prominent in the "RPS track" entries, where two-MIP (three-MIP) peaks at $\sim$ 6 000 (9 000) ADC counts are also discernible. The "No RPS track" entries show a smaller MIP peak and a broad plateau, which is attributed to "splash events" (see text).

F – MiniPlug contribution to $\xi_{\bar{p}}^{\rm CAL}$

G – Beam halo background

A. RPS dynamic alignment

The values of both ξ and t can be accurateley determined from RPS reconstructed track coordinates and the position of the event vertex at the Interaction Point (IP) using the beam transport matrix between the IP and RPS. Crucial for this determination is the detector X–Y alignment with respect to the beam. Below, we describe a method developed to dynamically determine the alignment of the RPS detectors during the RPS$_{\rm track}$ data collection period. The resulting $\xi_{\bar{p}}^{\rm RPS}$ distribution is used in Sec. V E to calibrate $\xi_{\bar{p}}^{\rm CAL}$.

The dynamic alignment method is illustrated in Fig. 4, where the curve represents a fit to the data (after alignment) with a form composed of two exponential terms,

$$\frac{d\sigma}{dt} = N_{norm} \cdot \left(A_1 \cdot e^{b_1 \cdot t} + A_2 \cdot e^{b_2 \cdot t}\right), \qquad (7)$$

where N_{norm} is an overall normalization factor.

Alignment is achieved by seeking a maximum of the $d\sigma/dt$ distribution at $t = 0$ for these events. The implementation of the alignment method consist of introducing software offsets $X_{\rm offset}$ and $Y_{\rm offset}$ in the X and Y coordinates of the RPS detectors with respect to the physical beam-line, and iteratively adjusting them until a maximum for $|d\sigma/dt|$ at $t = 0$ is found at the (X,Y) position where the RPS fiber tracker is correctly aligned. Results for such a fit are shown in Fig. 5. The accuracy in ΔX and ΔY of the RPS alignment calibration obtained using the inclusive data sample, estimated from Gaussian fits to the distributions in Fig. 5 around their respective minimum values, is ± 60 μm. This is limited only by the size of the data sample and the variations of the beam position during the time interval of data taking. The contribution of the latter is automatically folded into the the overall uncertainty.

B. RPS trigger efficiency

Due to radiation damage, the position of the minimum ionizing particle (MIP) peak of the three RPT counters shifts to smaller ADC values as the integrated luminosity of the data sample increases. The same behavior is

DRAFT

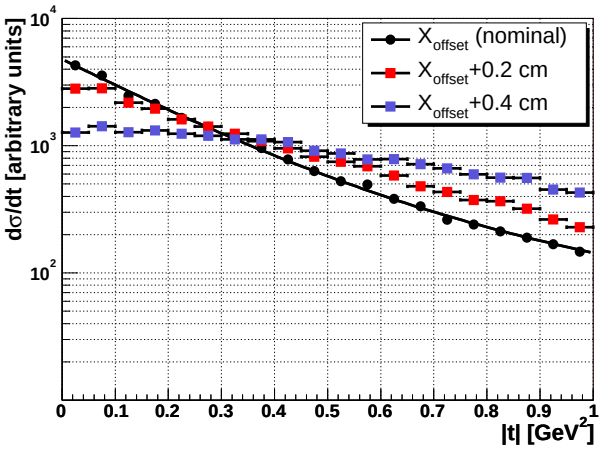


FIG. 4: $|t|$ distributions for SD–RPS–track events of reconstructed RPS tracks in the range $0 \leq |t| \leq 1$ GeV^2 for the nominal X position and for positive $X_{\rm offset}$ shifts relative to the beam line.

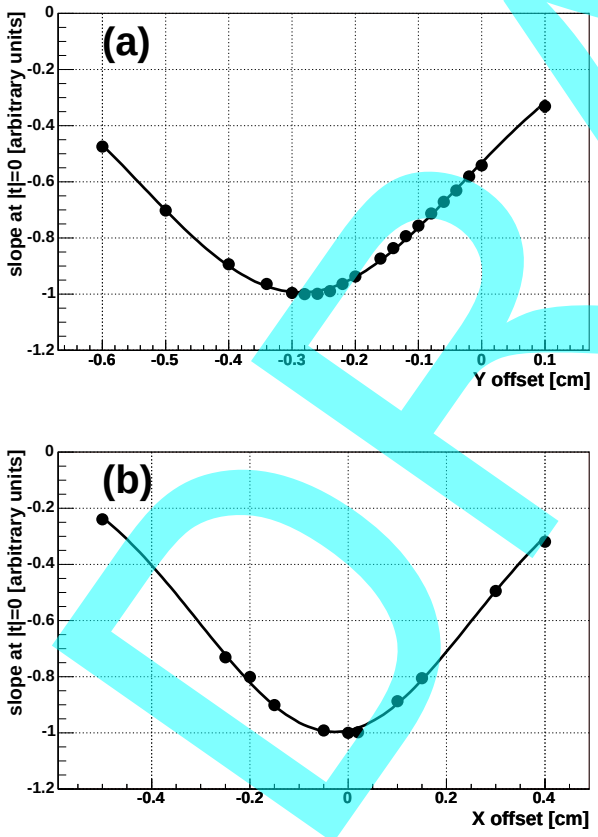


FIG. 5: The b_1 slope of the t-distribution parameterization of Eq. (7) vs. (a) $Y_{\rm offset}$ and (b) $X_{\rm offset}$ normalzed to its minimum value.

observed in all three trigger counters. As a direct consequence, the efficiency of the RPT triple coincidence decreases as a function of integrated luminosity. The RPT efficiency, ϵ_{RPT}, is measured from a sample of minimum bias (MB) data collected with a CLC$_p$·CLC$_{\bar{p}}$ coincidence trigger. The ADC distribution of each RPT counter was determined for different periods of data-taking by triggering with the other two RPT counters. Results are shown in Table II for 9 data sets of approximately equal integrated luminosity obtained by sub-dividing the MB data sample. The efficiency ϵ_{RPT} listed is calculated as the number of events with at least 1000 ADC counts in each RPT counter (the trigger requirement) divided by the number of events with at least 500 ADC counts in each counter, which is the lowest ADC value of the MIP peak found among all three counters in all data sets:

$$\epsilon_{RPT} = N_{1\cdot2\cdot3}(\mathrm{ADC} > 1000)/N_{1\cdot2\cdot3}(\mathrm{ADC} > 500). \quad (8)$$

An uncertainty of 10% is assigned to ϵ_{RPT} to account for variations due to the choice of the lowest ADC value of the MIP peak as determined from an analysis of the ADC distributions. The degradation of the RPT counters is taken into account by correcting the number of SD events for the RPT efficiency as a function of integrated luminosity.

TABLE II: Data sets, corresponding values of integrated luminosity, L, and triple-coincidence RPT counter efficiencies, ϵ_{RPT}.

Data set	L (pb^{-1})	ϵ_{RPT}
set 0	12.9	0.78 ± 0.08
set 1	24.0	0.75 ± 0.08
set 2	20.3	0.69 ± 0.07
set 3	6.4	0.57 ± 0.06
set 4	29.2	0.51 ± 0.05
set 5	16.3	0.46 ± 0.05
set 6	18.9	0.48 ± 0.05
set 7	25.5	0.43 ± 0.04
set 8	22.1	0.40 ± 0.04

C. Antiproton momentum loss measurement

The momentum loss of the $\bar{p}$ is calculated using the pseudorapidity η^i and transverse energy E_T^i of all the towers of the CCAL, PCAL, and MP calorimeters,

$$\xi_{\bar{p}}^{\rm CAL} = \frac{1}{\sqrt{s}} \sum_{i=1}^{N_{tower}} E_T^i e^{-\eta^i}, \quad (9)$$

where the sum is carried out over towers with $E_T >$ 100 MeV for CCAL and FCAL and $>$ 20 MeV for MP. Calibration issues of $\xi_{\bar{p}}^{\rm CAL}$ are addressed below in

DRAFT

Sec. V E. The resulting $\xi_{\bar{p}}^{\rm CAL}$ distributions are shown in Fig. 6. The filled circles in this figure represent the $\xi_{\bar{p}}^{\rm CAL}$ distribution of the entire RPS·Jet5 data sample after applying all the selection requirements listed in Table I. This distribution shows two peaks: one in the region of $\xi_{\bar{p}}^{\rm CAL} \lesssim 10^{-1}$ labeled SD, and a broader one at $\xi_{\bar{p}}^{\rm CAL} \gtrsim 10^{-1}$ labeled BG (background). The data points represented by filled squares are from the inclusive Jet5 data sample normalized (rescaled) to the number of the RPS·Jet5 events in the BG region, and those represented by filled stars are from the RPS(w/track)·Jrt5 data sample of events with a reconstructed RPS track normalized (rescaled) to the number of RPS·Jet5 events in the SD region.

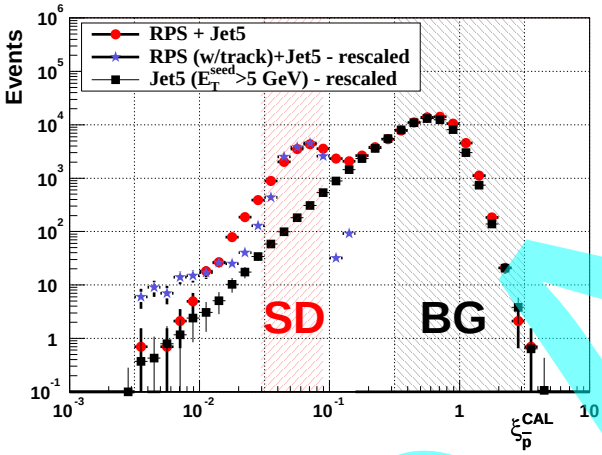


FIG. 6: The distribution of calorimeter measured antiproton momentum loss fraction $\xi_{\bar{p}}^{\rm CAL}$ for three data samples: (a) RPS·Jet5 (filled circles), (b) RPS(w/track)·Jet5-rescaled (filled stars), and (c) Jet5-rescaled (filled squares). The regions labeled SD and BG are respectively dominated by SD and background evens consisting of a ND dijet event and a SD event that provides the RPS trigger. The RPS(w/track)·Jet5 and Jet5 distributions are normalized to the RPS·Jet5 distribution in the SD and BG regions, respectively.

The RPS·Jet5 data distribution is interpreted as follows:

b. Single diffractive region. The events in the SD region are mainly due to SD dijet production. The declining trend of the distribution below $\xi_{\bar{p}}^{\rm CAL} \sim 0.05$ occurs in the region where the RPS acceptance is decreasing.

c. Background region. The events in the BG region, which form the broad peak centered at $\xi_{\bar{p}}^{\rm CAL} \sim 0.5$, are mainly due to overlaps of a ND dijet event and a soft diffractive interaction that triggered the RPS but yielded no reconstructed vertex. A negligibly small fraction of the events in this region are due to SD dijet events superimposed with a MB event. Both types of overlap events should yield a value of $\xi_{\bar{p}}^{\rm CAL} = 1$, but the expected δ-function is smeared by the resolution of the energy measurement in the calorimeters and shifted toward lower ξ-values by particles escaping detection either in the areas of the calorimeter interfaces or due to the imposed energy thresholds.

As the rate of overlap events increases with instantaneous luminosity $\mathcal{L}$, the ratio of BG/SD events in the $\xi_{\bar{p}}^{\rm CAL}$ distribution of the RPS+Jet5 event sample is expected to decrease with decreasing $\mathcal{L}$. This effect is observed in the RPS·Jet5 data when binned in intervals of different $\mathcal{L}$ (not shown in Fig. 6).

d. Diffractive events. The excess of the RPS·Jet5 events over Jet5 distribution in the SD region is mainly due to diffractive production. The fraction of ND events in the region of $0.03 < \xi_{\bar{p}}^{\rm CAL} < 0.09$ is $\sim 12\%$. As the RPS acceptance depends on both $\xi_{\bar{p}}$ and t, and t is not measured for each event, the background from ND events in the SD region is accounted for in a simple MC simulation designed to calculate the acceptance on an event-by-event basis. Inputs to this simulation are the ξ and t distributions measured from data in which RPS tracking was available. Each event generated within a given bin of $\xi^{\rm RPS}$ is weighted by a factor equal to the ratio of the total number of events over the number of SD signal events in the corresponding $\xi_{\bar{p}}^{\rm CAL}$ bin of the RPS·Jet5 data plotted in Fig. 6.

D. Multiple interactions

Multiple interaction effects are handled by using the fraction of one-interaction events in the data sample to normalize the SD/ND event ratio in a multiple interaction environment. This fraction is estimated from a Pythia Monte Carlo generated sample of events containing the appropriate run-dependent fraction of multiple interactions for each run. The ratio of the number of one-interaction events $N^{\rm 1_int}$ to all events $N^{\rm all}$ decreases with increasing $\mathcal{L}$ following a distribution well described by an exponential expression:

$$f^{\rm 1_int} \equiv \frac{N^{\rm 1_int}}{N^{\rm all}} \propto \exp[-c\cdot\mathcal{L}];\ c = -0.34\pm0.06\ cm^2 sec\cdot 10^{-31}. \quad (10)$$

Applying a vertex cut would eliminate a large fraction of ND overlap events, but might also reject diffractive events due to vertex reconstruction inefficiencies which depend on the event activity and therefore on both the ξ-value and the multiple interaction content. To avoid biasing the ξ-distribution we apply no vertex cut and correct for the ND overlap event contamination in evaluating cross sections.

E. Calibration of $\xi_{\bar{p}}^{\rm CAL}$

The measurement of $\xi_{\bar{p}}^{\rm CAL}$ using Eq. (9) is calibrated by comparing the values obtained with those measured by the RPS, $\xi_{\bar{p}}^{\rm RPS}$. The comparison is made using an event

DRAFT

sub-sample for which tracking information is available. The $\xi_{\bar{p}}^{\rm RPS}$ distribution for these events is shown in Fig. 7.

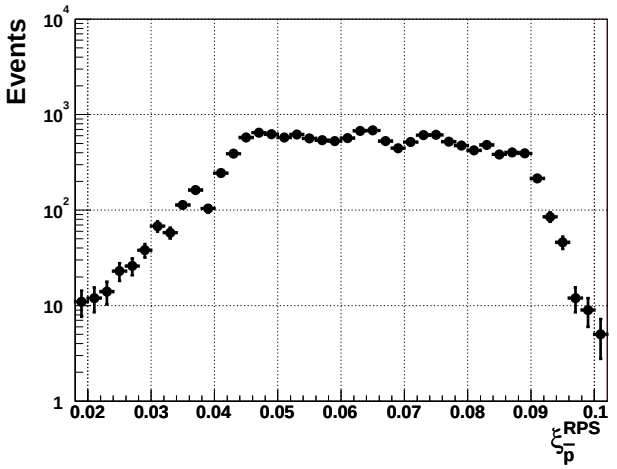


FIG. 7: Distribution of antiproton momentum loss fraction $\xi_{\bar{p}}^{\rm RPS}$ for events with a reconstructed RPS track from an event sub-sample for which RPS tracking is available.

Figure 8 shows a two-dimensional scatter plot of $\xi_{\bar{p}}^{\rm CAL}$ vs. $\xi_{\bar{p}}^{\rm RPS}$ for the events with a reconstructed RPS track. An approximately linear relationship between $\xi_{\bar{p}}^{\rm CAL}$ and $\xi_{\bar{p}}^{\rm RPS}$ is observed along the peak of the distribution of entries in the region of $\xi_{\bar{p}}^{\rm CAL} \lesssim 0.1$ and $0.03 \lesssim \xi_{\bar{p}}^{\rm RPS} \lesssim 0.09$, where the diffractive events are expected. As already discussed, the entries with $\xi_{\bar{p}}^{\rm CAL} > 0.1$ are mainly due to ND dijet event with a superimposed soft SD overlap event. Without the measurement of $\xi_{\bar{p}}^{\rm CAL}$ the overap events would contribute a large and inseparable background to the SD events.

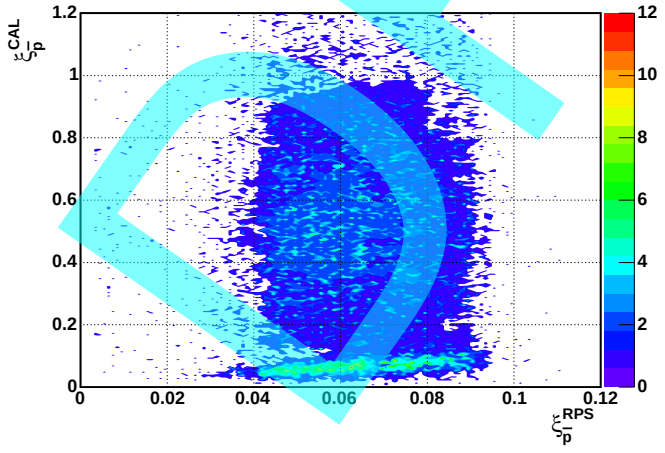


FIG. 8: Two-dimensional scatter plot of $\xi_{\bar{p}}^{\rm CAL}$ vs. $\xi_{\bar{p}}^{\rm RPS}$ for all events in the data sub-sample for which RPS tracking is available.

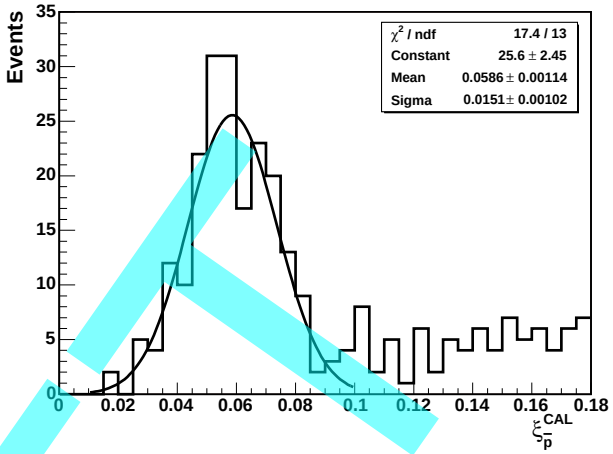


FIG. 9: The distribution of antiproton fractional momentum loss $\xi_{\bar{p}}^{\rm CAL}$ for events with $\xi_{\bar{p}}^{\rm RPS}$ in the range $0.055 < \xi_{\bar{p}}^{\rm RPS} < 0.060$. The bell-shaped curve is a Gaussian fit in the region of $\xi_{\bar{p}}^{\rm CAL} < 0.1$.

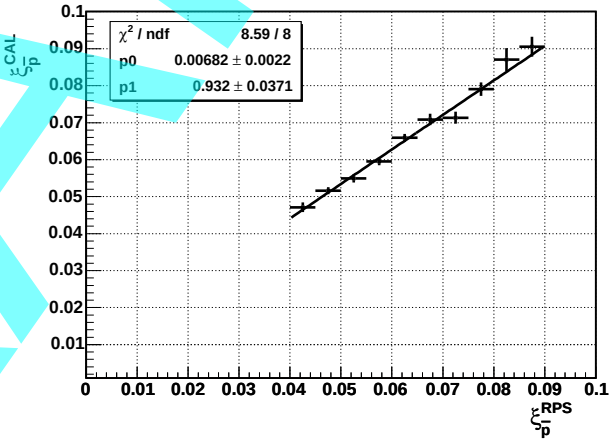


FIG. 10: Median values of $\xi_{\bar{p}}^{\rm CAL}$ obtained from fits to data in different $\xi_{\bar{p}}^{\rm RPS}$ bins. A linear fit (line) in the region $0.045 < \xi_{\bar{p}}^{\rm RPS} < 0.090$ well describes the data.

For a quantitative calibration of $\xi_{\bar{p}}^{\rm CAL}$ the data are divided into bins of width $\Delta\xi_{\bar{p}}^{\rm RPS} = 0.005$ and the $\xi_{\bar{p}}^{\rm CAL}$ values in each bin are fitted with a Gaussian distribution. Figure 9 shows such a fit for the bin of $0.055 < \xi_{\bar{p}}^{\rm CAL} < 0.050$. The ratio of the half-width to the average value of the fittted curve is found to have the constant value of $\delta\xi_{\bar{p}}^{\rm CAL}/\xi_{\bar{p}}^{\rm CAL} \approx 0.3$ over the entire $\xi_{\bar{p}}^{\rm CAL}$ range of this data sample.

The results of $\xi_{\bar{p}}^{\rm CAL}$ vs. $\xi_{\bar{p}}^{\rm RPS}$ for all the $\Delta\xi_{\bar{p}}^{\rm CAL}$ bins within the plateau region of $0.04 < \xi_{\bar{p}}^{\rm RPS} < 0.09$ of the $\xi_{\bar{p}}^{\rm CAL}$ distribution of Fig. 7 are plotted in Fig. 10. A linear relationship is observed of the form $\xi_{\bar{p}}^{\rm CAL} = p^0 + p1 \cdot \xi_{\bar{p}}^{\rm RPS}$

DRAFT

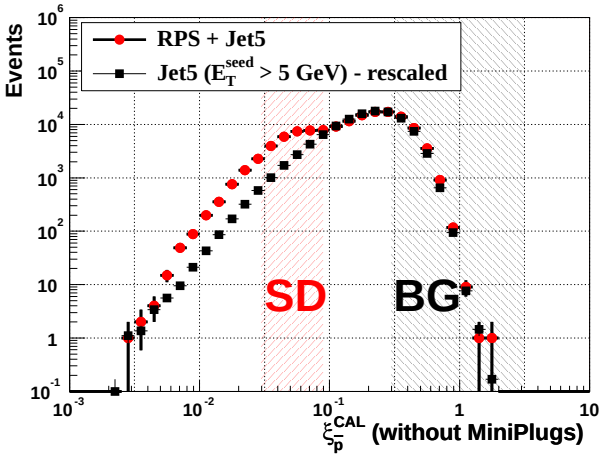


FIG. 11: The $\xi_{\bar{p}}^{\rm CAL}$ distribution for RPS·Jet5 and Jet5 data evaluated without the MiniPlug calorimeter contributions. The diffractive peak is less discernible in the RPS·Jet5 distribution and the Jet5 background is larger than in Fig 6 where the MiniPlugs are included in the evaluation of $\xi_{\bar{p}}^{\rm CAL}$.

with $p^0 = 0.007 \pm 0.002$ and $p1 = 0.97 \pm 0.04$ as compared to the ideal values of $p^0 = 0$ and $p1 = 1$.

F. MiniPlug contribution to $\xi_{\bar{p}}^{\rm CAL}$

The measured value of $\xi_{\bar{p}}^{\rm CAL}$ receives contributions from all the CDF calorimeter sub-systems. The largest contribution at large $\xi_{\bar{p}}$ comes from PCAL$_{\bar{p}}$ and MP$_{\bar{p}}$. The contribution of the MP$_{\bar{p}}$ is particularly important for reducing the background due to ND dijet events overlapped by a soft SD recoil $\bar{p}$ detected in the RPS. Figure 11 shows the $\xi_{\bar{p}}^{\rm CAL}$ distribution for the RPS·Jet5 and Jet5 data without the contribution from the MP calorimeters. In comparison with Fig. 6, the BG peak is shifted towards the SD region and contributes a considerably larger ND background to the SD events.

The MP calibration was performed by comparing E_T distributions between data and Monte Carlo generated events. The slopes of the dN/dE_T distributions of the data were first equalized among the MP towers within a given polar angular range (η-ring), and then normalized to the corresponding slopes obtained from Monte Carlo generated events that ended up in that η-ring. The resolution in the measurement of E_T was estimated to be $\delta E_T = \pm 30\%$ using data obtained with a MP prototype calorimeter placed in high energy positron and pion beams [39] . Varying the MP energy by $\pm$ 30% shifts $\log\xi$ by $\Delta\log\xi = \pm 0.1$, which is comparable to the bin width used in the analysis (see Fig. 6).

G. Beam halo background

The background in the $\xi_{\bar{p}}^{\rm CAL}$ distribution due to beam halo was studied using a trigger provided by the machine clock at the nominaltime the $\bar{p}$ and p beam bunches cross the $z = 0$ position at the center of CDF II regardless of whether or not there is a $\bar{p}p$ interaction. This trigger, which is referred to as "zeor-crossing," leads to different data samples depending on additional conditions that may be imposed.

Three zero-crossing event samples were analyzed:

(a) zero-crossing inclusive;

(b) zero-crossing events with no reconstructed vertex;

(c) zero-crossing events with a RPS trigger requirement.

Figure 12 shows the $\xi_{\bar{p}}^{\rm CAL}$ distribution for these samples. Three regions of $\xi_{\bar{p}}^{\rm CAL}$ are of interest: (a) $\xi_{\bar{p}}^{\rm CAL} > 0.1$, where ND events dominate, (b) $10^{-3} < \xi_{\bar{p}}^{\rm CAL} < 0.1$, where SD events are expected, and (c) $\xi_{\bar{p}}^{\rm CAL} < 10^{-3}$, where "empty" events with one to a few CCAL or FCAL towers above threshold due to beam halo particles and/or due to calorimeter noise may contribute to $\xi_{\bar{p}}^{\rm CAL}$.

The contribution of a single CCAL or FCAL tower at $\eta = 0$ with $E_T = 0.2$ GeV (the threshold used) is estimated from Eq. 9 to be $\xi_{\bar{p}}^{\rm CAL} = 1 \times 10^{-4}$, which is well below the ξ-range of the RPS acceptance. At $\xi_{\bar{p}}^{\rm CAL} \sim 3 \times 10^{-4}$, we observe a backround peak corresponding to an average of ~ 3 CCAL towers at an event rate of $\sim 5\%$ of the diffractive signal concetrated at $\xi_{\bar{p}}^{\rm CAL} \sim 0.05$. We estimate that an upward fluctuation by a factor of 100 would be required for this background to compete with the overlap backround already present within the diffractive region of $0.03 < \xi_{\bar{p}}^{\rm CAL} < 0.09$. Because of the negligible probability of such a fluctuation, no correction is applied to the data for beam halo background.

VI. RESULTS

Our results are presented in three sub-sections. In VI A we discuss certain kinematic distributions that establish the diffractive nature of the events in our data samples, in VI B we present ratios of SD to ND production rates and extract the diffractive structure function, and in VI C we report results on t-distributions.

A. Kinematic distributions

The presence of a rapidity gap in diffractive events leads to characteristic kinematic distributions. Here, we compare the SD and ND distributions of mean transverse jet energy $E_T^* = (E_T^{jet1} + E_T^{jet2})/2$, mean jet pseudorapidity $\eta^* = (\eta^{jet1} + \eta^{jet2})/2$, jet azimuthal angle difference $\Delta\phi = |\phi^{jet1} - \phi^{jet2}|$, and MiniPlug multiplicity.

DRAFT

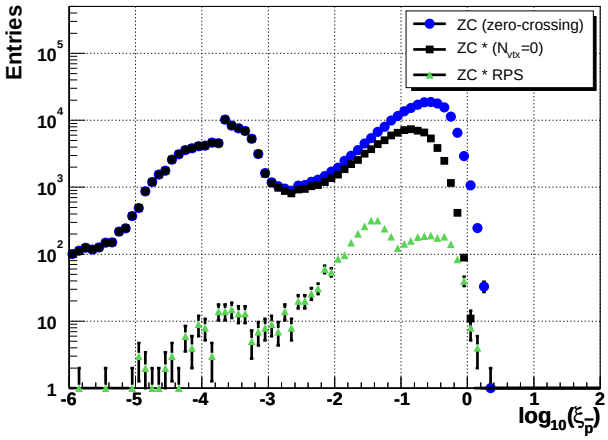


FIG. 12: The $\xi_{\bar{p}CAL}$ distribution in zero-crossing (ZC) events (circles), ZC with no reconstructed vertices (squares), and ZC with a RPS trigger (triangles).

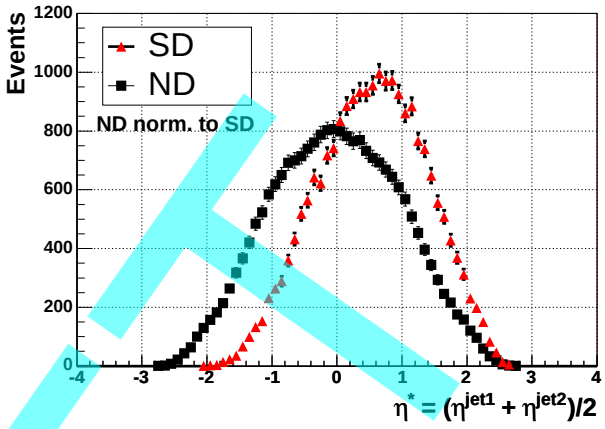


FIG. 14: The average η distribution $\eta^* = (\eta^{\rm jet1} + \eta^{\rm jet2})/2$ of the two highest E_T jets for SD and ND events. The ND distribution is normalized to the total number of SD events.

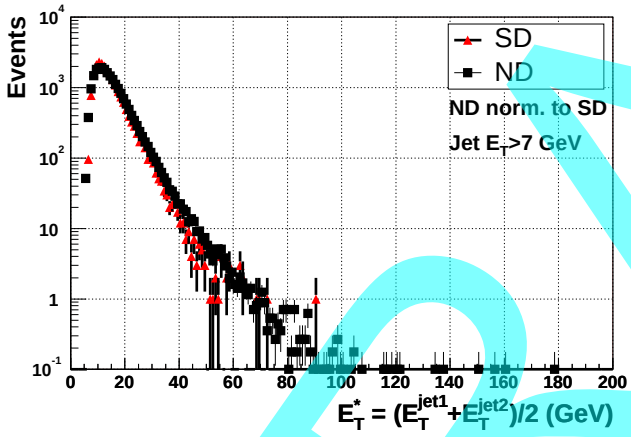


FIG. 13: The distribution of the mean dijet transverse energy $E_T^* = (E_T^{\rm jet1} + E_T^{\rm jet2})/2$ for SD and ND events. The ND distribution is normalized to the total number of SD events.

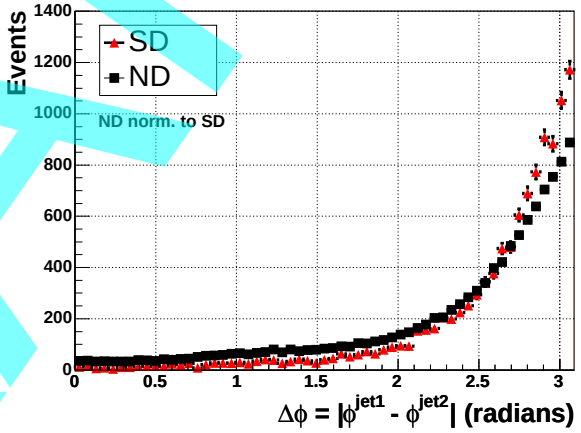


FIG. 15: The distribution of the azimuthal angle difference $\Delta\phi$ between the two highest E_T jets for SD and ND events. The ND distribution is normalized to the total number of SD events.

a. Transverse jet energy The mean dijet transverse energy, $E_T^* = (E_T^{jet1} + E_T^{jet2})/2$, is presented in Fig. 13 for SD and ND events. The total number of ND events is normalized to that of the SD events and the associated statistical uncertainties rescaled. The SD and ND distributions are very similar. The slightly narrower width of the SD distribution is attributed to the lower effective c.m.s. energy and to the larger content of forward jets, which tend to have a lower average E_T [27].

b. Jet pseudorapidity The mean dijet pseudorapidity distribution of the two leading jets, $\eta^* = (\eta^{jet1} + \eta^{jet2})/2$, is shown in Fig. 14 for SD and ND events. The ND events are centered around $\eta^\star = 0$, while the SD distribution is shifted towards positive values (i.e. in the proton beam direction) due to the boost of the c.m.s. of the $I\!P$-p collision.

c. Azimuthal angle correlations The distributions of the azimuthal angle difference between the two leading jets, $\Delta\phi = |\phi^{jet1} - \phi^{jet2}|$, are shown in Fig. 15 for SD and ND events. The SD dijets are more back-to-back than the ND ones, as would be expected from the reduced available sub-energy of the diffractive system.

d. MiniPlug multiplicity The $\mathrm{MP}_{\bar{p}}$ multiplicity distribution for SD and ND events is shown in Fig. 16. Multiplicities are evaluated by counting the number of peaks above calorimeter tower noise levels using "seed" towers with a minimum transverse energy of 20 MeV [30]. Such peaks originate from three sources: (a) charged hadrons traversing the MP without interacting, (b) charged and

DRAFT

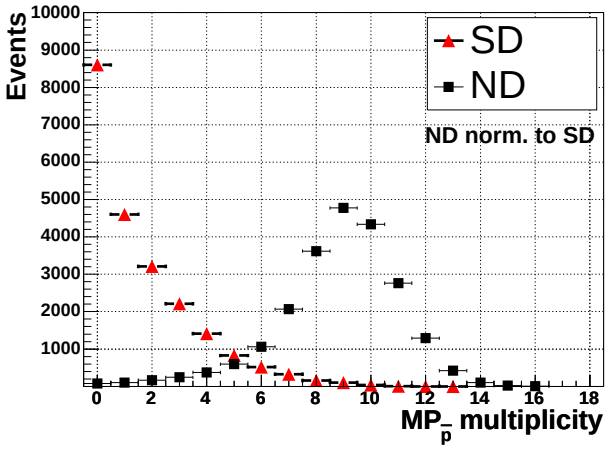


FIG. 16: The multiplicity distribution in the $MP_{\bar{p}}$ calorimeter for SD and ND events.The ND distribution is normalized to the total number of SD events.

neutral hadrons interacting in the material of the MP plates, and (c) electro-magnetic energy deposited by $e^{+/-}/\gamma$'s. The SD events have smaller multiplicites in comparison with the ND events, as expected from the reduced c.m.s. energy of the Pomeron-proton relative to the $p\bar{p}$ collision.

B. Ratio of SD to ND production rates and the diffractive structure function

The ratio $\mathcal{R} \equiv R_{SD/ND}(x,\xi,t)$ of the SD to ND dijet production rates, which in LO QCD is proportional to the ratio of the corresponding structure functions (see Sec. II), is measured as a function of the Bjorken scaling variable $x_{Bj}^{\bar{p}}$ of the struck parton of the antiproton and the 4-momentum transfer squared $Q^2 \approx \langle E_T^* \rangle^2$. For each event, $x_{Bj}^{\bar{p}}$ is evaluated from the E_T and η values of the jets using the formula

$$x_{Bj}^{\bar{p}} = \frac{1}{\sqrt{s}} \sum_{i=1}^{3-\text{jets}} E_T^i e^{-\eta^i}, \qquad (11)$$

where the sum is carried out over the two leading jets plus a third jet of $E_T > 5$ GeV, if present. Theoretically, the sum should be over all jets in the final state, but the fraction of events with more than three jets of $E_T > 5$ GeV is relatively small and including them in the evaluation of $x_{Bj}^{\bar{p}}$ does not significantly affect the obtained results [27].

Jet energies are measured using a cone algorithm based on measuring the "visible" energy deposited in the detector within a cone of radius $R_{\text{cone}} = \sqrt{\delta\eta^2 + \delta\phi^2} = 0.7$ and applying appropriate corrections [26]. Both the SD and ND jets contain within the jet cone an amount of underlying event (UE) energy from soft spectator partonic interactions, which we subtract from the measured jet energy. For diffractive events, where a large fraction of the event energy is carried away by the recoil antiproton, the amount of UE energy is expected to be smaller than in ND events.

The UE energy in SD events was measured using the sample of RPS inclusive triggered data. To suppress overlap backgrounds, we required the events to be in the region of $0.01 < \xi_{\bar{p}}^{\text{CAL}} < 0.14$, which is dominated by SD events from a single $\bar{p}p$ interaction. We then selected events with only one reconstructed vertex with $|z_{\text{vtx}}| < 60$ cm ($\sim 1\,\sigma$) and measured the ΣE_T of all central calorimeter towers within a randomly chosen cone of radius $R_{\text{cone}} = 0.7$ in the region $0.1 < |\eta| < 0.7$. The UE energy in MB (ND dominated) events was also measured using the random cone technique. From these two measurements we obtained an average UE E_T of 0.90 GeV (1.56 GeV) for SD (ND) events.

1. x_{Bj} dependence

The ratio $\mathcal{R}$ of the number of SD dijet events per unit ξ over the number of ND events of the Jet5 sample is corrected for the effect of multiple interactions and for the RPS detector acceptance.

To account for multiple interactions contributing to the ND sample, the ND x_{Bj} distribution is weighted by the factor $f^{1\text{-int}} = \exp[-c \cdot \mathcal{L}]$, where $\mathcal{L}$ is the instantaneous luminosity and $c = -0.34 \pm 0.06\ cm^2 sec \cdot 10^{-31}$ (see Sec. V D). This correction is not applied to the SD events, since contributions from additional interactions shift $\xi_{\bar{p}}^{CAL}$ into the BG region.

The number of SD events is corrected for the RPS acceptance, which is estimated from a beam-optics simulation to be $\epsilon_{RPS} = 0.80 \pm 0.04$ (syst.) [18], and the obtained SD and ND data samples are normalized to their respective integrated luminosities.

The results for the ratio $\mathcal{R}$ for events within $0.03 < \xi < 0.09$ are presented in Fig. 17 as a function of $\log_{10} x_{\text{Bj}}$ along with the results obtained in Run I for $0.035 < \xi < 0.095$ and $|t| < 1$ GeV^2 [10]. Both the Run I and Run II results have an estimated $\pm 25\%$ systematic uncertainty in the overall normalization [10]. The shapes of the two distributions are in good agreement, except in the high x_{Bj} region where the Run I distribution is seen to extend to higher x_{Bj} values. This behavior is expected from the difference in $\langle E_T^* \rangle$ and η acceptance for jets in RunI (Run II), which is $\langle E_T^* \rangle \approx 7$ GeV (12 GeV) GeV and $|\eta| < 3.7$ ($|\eta| < 2.7$). This difference results in a larger x_{Bj} reach in Run I by a factor of $(12/7) \times e^{3.7-2.7} \approx 2$, as estimated using Eq. 11.

A fit to all Run II data in the range $0.03 < \xi < 0.09$ using the form $\mathcal{R} = \mathcal{R}_\circ \cdot x_{Bj}^r$ subject to the constraint $\beta = (x/\xi) < 0.5$ [10] yields $r = -0.44 \pm 0.04$ and $\mathcal{R}_\circ = (8.6 \pm 0.8) \times 10^{-3}$. This result is compatible with the Run I result of $r = -0.45 \pm 0.02$ and $\mathcal{R}_\circ = (6.1 \pm 0.1) \times 10^{-3}$ obtained by a constrained fit of the form $\mathcal{R} = \mathcal{R}_\circ \cdot$

DRAFT

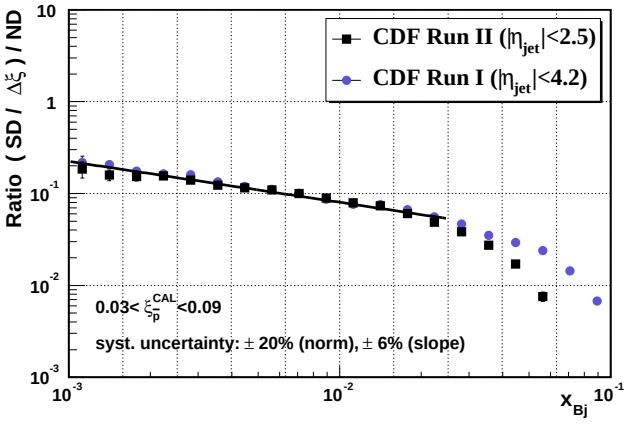


FIG. 17: The ratio of diffractive to non-diffractive dijet event rates as a function of $x_{\rm Bj}$. The quoted overall systematic uncertainty of ±20 % is due to the uncertainties $\Delta\mathcal{R}_0$ and Δr listed in table III.

$(x_{Bj}/0.0065)^r$ designed to match the data at the average value of $x_{Bj}/0.0065$, which accounts for the lower $\mathcal{R}_\circ$ value.

The systematic uncertainties in $\mathcal{R}_\circ$ and r are listed in Table III. The causes of uncertainty investigated include the underlying event, the energy scale, the calorimeter tower E_T thresholds, overlaps in ND events, instantaneous luminosity $\mathcal{L}$, bunch-by-bunch variation in $\mathcal{L}$, RPS acceptance, and "spash" events.

a. Underlying event The underlying event energy is subtracted from the jet energy when the jet energy corrections are applied. The results presented are for a ±30% variation of the UE energy correction, which is sufficient to cover the uncertainty for jets depositing energy near the interfaces or the outer edges of a calorimeter.

b. Energy scale The effect of the energy scale of the CCAL, PCAL and MP calorimeters on $\xi_{\bar{p}}^{\rm CAL}$ and thereby on $\mathcal{R}_\circ$ and r was estimated by changing the CCAL and PCAL jet energies by ±5% and the MP tower energies by ±30%. These values were obtained from detailed studies of relevant data samples.

c. Tower E_T threshold Tower energy threshold effects would generally be expected to cancel out in measuring the ratio of rates. However, due to the different UE event contributions in SD and ND events, the tower thresholds applied could affect the result. The uncertainty in $\mathcal{R}$ for jets with mean transverse energy of $E_T^* > 10$ GeV ($E_T^* > 12$ GeV) due to tower threshold effectes is estimated to be +1% (+2%). The effect on both $\mathcal{R}_\circ$ and on r for our total SD event sample is ±1%.

d. Overlaps in ND events To account for event overlaps in ND events occurring at high instantaveous luminosities the ND, each event is weighted by a factor of $w = \exp[n \cdot \mathcal{L}]$, where $n = -0.34 \pm 0.06\ cm^2 sec \cdot 10^{-31}$ (see sec. V D). The uncertainty in n has a ±8% effect on the determination of $\mathcal{R}_\circ$.

e. Instantaneous luminosity $\mathcal{L}$ We estimate an uncertainty of ±3% in the determination of $\mathcal{R}_\circ$ due to a variation of ±6% in $\mathcal{L}$ during the data collection period.

f. Bunch-by-bunch variation in $\mathcal{L}$ A bunch-by-bunch variation of ∼50% in $\mathcal{L}$ over the collection of our data sample contributes a ±4% systematic uncertainty in $\mathcal{R}_\circ$.

g. RPS acceptance Using a MC simulation, the uncertainty in $\mathcal{R}_\circ$ was estimated to be ±10%.

h. Splash events By evaluating the differences among data sub-samples, a systematic uncertainty of ±6% is estimated due to the cut applied to remove the splash events (see Table IV).

Added in quadrature, the above uncertainties yield $\Delta\mathcal{R}$ (syst.) = ±18 % and Δr (syst.) = ±6 %.

TABLE III: Systematic uncertainties $\Delta\mathcal{R}_\circ$ and Δr in $\mathcal{R}_\circ$ and r of the ratio of SD to ND events parameterized as $\mathcal{R} = \mathcal{R}_\circ \cdot x_{Bj}^r$. The uncertainties are estimated either by varying the parameter associated with the source of error by an amount denoted by "Variation," or in the cases marked as "N/A" (not applicable) by a direct calculation using data or simulated event distributions as explained in the text.

Source of uncertainty	Variation	$\Delta\mathcal{R}_\circ$	Δr
underlying event	±30%	±3%	∓5%
central/plug cal. energy scale	±5%	±8%	∼3%
MiniPlug energy scale	±30%	∓6%	±1%
tower E_T threshold	±10%	±1%	±1%
overlaps in ND events	±20%	±8%	$<$ ±1%
instantaneous luminosity	±6%	±3%	N/A
bunch by bunch luminosity	±50%	±4%	N/A
RPS acceptance	N/A	±10%	N/A
splash events	N/A	±6%	N/A
Total uncertainty		±18%	±6%

2. Q^2 dependence

As discussed in Sec. IV, special data samples collected with dedicated triggers are used to extend the measurement of the jet energy spectrum to E_T^{jet} ∼100 GeV. Results for the ratio $\mathcal{R}$ obtained from an analysis of these samples similar to that described above are presented in Fig. 18 for $Q^2 \equiv \langle E_T^* \rangle^2$ in the range of $\sim 100 < Q^2 < 10^4$ (GeV/c)^2. These distributions are only affected by the overall uncertainty in normalization, as the relative uncertainties between different Q^2 bins cancel out in measuring the ratio. A factor of $\lesssim 2$ variation among all distributions is observed over the entire Q^2 range, as compared to a factor of $\sim 10^4$ over the same range between the individual SD and ND distributions shown in Fig. 13. The results of fits performed using the form $\mathcal{R} = \mathcal{R}_\circ \cdot x_{Bj}^r$ in the region $0.001 < x_{Bj} < 0.025$, where the constraint $\beta = (x/\xi) < 0.5$ is satisfied, are presented for different jet E_T^* intervals in Table IV. Both $\mathcal{R}_0$ and r are constant within the uncertainties over the entire range of

DRAFT

BLESS

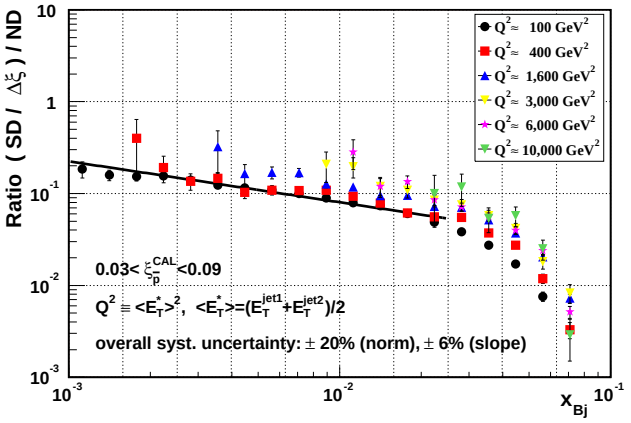


FIG. 18: The ratio of diffractive to non-diffractive dijet event rates as a function of $x_{\rm Bj}$ (momentum fraction of parton in the antiproton) for different values of $Q^2 \equiv \langle E_T^* \rangle^2$. The quoted overall systematic uncertainy of ±20 % is due to the uncertainties $\Delta\mathcal{R}_0$ and Δr listed in table III.

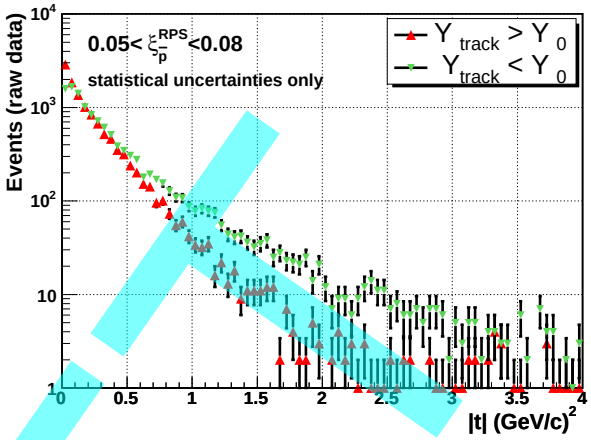


FIG. 19: **[Vertical axis: Events per $\Delta t = 0.05$]** t-distributions of SD⊕RPS$_{\rm track}$ events with $0.05 < \xi_{\bar{p}}^{RPS} < 0.08$ for $Y_{track} > Y_0$ (triangles) and $Y_{track} < Y_0$ (circles), where Y_0 is the centerline of the RPS fiber tracker.

$10^2 < Q^2 < 10^4$ (GeV/c)^2. This result indicates that the Q^2 evolution in diffractive interactions is similar to that in ND interactions [42].

TABLE IV: Fit parameters of the ratio of SD/ND production rates for events in different E_T^* bins. The ratios are fitted to the form $\mathcal{R} = \mathcal{R}_\circ \cdot x_{Bj}^r$ in the range of $0.001 < x_{Bj} < 0.025$.

Jet E_T^* [GeV]	Q^2 (GeV/c)^2)	$\mathcal{R}_\circ$	r
$8 < E_T^* < 12$	100	$(8.6 \pm 0.8) \times 10^{-3}$	-0.44 ± 0.04
$18 < E_T^* < 25$	400	$(8.0 \pm 1.6) \times 10^{-3}$	-0.48 ± 0.05
$35 < E_T^* < 50$	1,600	$(6.3 \pm 1.8) \times 10^{-3}$	-0.60 ± 0.07
$50 < E_T^* < 70$	3,000	$(5.5 \pm 5.0) \times 10^{-3}$	-0.64 ± 0.22
$70 < E_T^* < 90$	6,000	$(7.0 \pm 7.0) \times 10^{-3}$	-0.58 ± 0.26

BLESS

C. t-distribution

The t-distribution was measured for two data samples, the SD⊕RPS$_{\rm track}$ (RPS, circles) and the SD⊕RPS$_{\rm track}$·Jet5 (RPS·Jet5, triangles). In Sec. VI C 1, we discuss the t-distribution in the region of $0 < |t| < 1$ (GeV/c)^2 as a function of jet $\langle E_T^* \rangle^2 \equiv Q^2$ and extract the dependence of the slope parameter at $|t| \approx 0$ as a function of Q^2; and in Sec. VI C 3, we examine the shape of the t-distribution in the region up to $|t| = 4$ (GeV/c)^2 and search for a diffraction minimum. Crucial for the measurement at $|t| > 4$ (GeV/c)^2 is the background subtraction.

a. Background evaluation The background was evaluated from the data by taking advantage of the asymmetric placement of the RPS detectors during data taking. As shown in Fig. 5, the dynamic alignment method yields $Y_{\rm offset} \approx 0.25$ cm and $X_{\rm offset} \approx 0$. The non-zero value of $Y_{\rm offset}$ results in an asymmetric t-range in the acceptance. Since the RPS detectors are 2 cm wide, and given that $t \propto -\theta_{\bar{p}}^2$ where $\theta_{\bar{p}} \propto Y_{\rm offset}$, the $|t|$-range of the RPS acceptance is expected to be a factor of $[(1+0.25)/(1-0.25)]^2 = 2.8$ larger in the $Y_{\rm track} > Y_0$ than in the $Y_{\rm track} < Y_0$ region, where Y_0 is the $Y = 0$ centerline of the detector.

Figure 19 shows t-distributions of SD⊕RPS$_{\rm track}$ data for $0.05 < \xi_{\bar{p}}^{RPS} < 0.08$. Two distributions are shown, one for $Y_{\rm track} > Y_0$ and the other for $Y_{\rm track} < Y_0$. The $Y_{\rm track} > Y_0$ distribution falls exponentially down to $|t_1| \approx 2.3$ (GeV/c)^2 and becomes consistent with an average flat value of $N_{bg} = 2/(\text{GeV/c})^2$ in the unphysical region of $|t| > |t_1|$. We have verified that the event rate at $|t| > |t_1|$ scales with that at $|t| \sim 0$ for runs with different instantaneous luminosities and conclude that these events represent a background associated with a $\bar{p}p$ interaction. However, since the reconstructed track is outside the RPS acceptance, its origin appears to be a particle from the $\bar{p}p$ interaction that suffered a collision before reaching the PPS and either it or another particle originating from this collision traversed the RPS. Such secondary collisions would be expected to produce a flat distribution in the vicinity of the RPS in a plane perpendicular to the beam, consistent with the flat distribution observed at $|t| > 2.5$ (GeV/c)^2 for $Y_{\rm track} > Y_0$.

Based on the estimated values of $|t_1| \approx 2.3$ (GeV/c)^2 and the scaling factor of 2.8 for the detector vertical misalignment, the unphysical region for the $Y_{\rm track} < Y_0$ data is expected to lie at $|t| > |t_2|$, where $|t_2| = 2.3 \times 2.8 = 6.5$ (GeV/c)^2. However, to reduce systematic uncertainties arising from edge-effects we present t-distributions only $|t| \leq 4$ (GeV/c)^2 (see Sev. VI C 3).

DRAFT

TABLE V: Slopes of t-distributions for soft and hard diffractive events of the SD⊕RPS$_{\rm track}$ data in the range $0.05 < \xi_{\bar{p}}^{\rm RPS} < 0.09$ for different $\langle E_T^* \rangle$ or $Q^2 \equiv \langle E_T^* \rangle^2$ bins obtained from fits to the form of Eq. (7), $d\sigma/dt = N \cdot (A_1 \cdot e^{b_1 \cdot t} + A_2 \cdot e^{b_2 \cdot t})$, with $A_2/A_1 = 0.11$ (see text). The uncertainties listed are statistical.

Event-ample	$\langle E_T^* \rangle$ GeV	Q^2 $(GeV/c)^2$	$-b_1$ $(GeV/c)^{-2}$	-b_2 $(GeV/c)^{-2}$	$b_1/b_1^{\rm incl}$ ratio	$b_2/b_2^{\rm incl}$ ratio
RPS	incl	≈ 1	6.6 ± 0.1	1.5 ± 0.1	1.00 ± 0.02	1.00 ± 0.03
RPS·Jet5	15	225	6.1 ± 0.5	1.6 ± 0.2	0.93 ± 0.07	1.08 ± 0.12
RPS·Jet20	30	900	6.2 ± 0.4	1.4 ± 0.1	0.94 ± 0.06	0.95 ± 0.09
RPS·Jet50	67	4500	6.8 ± 0.8	1.3 ± 0.2	1.04 ± 0.09	0.87 ± 0.12

BLESS

b. Corrections The data are corrected by subtracting the background and dividing by the RPS acceptance. This is performed on an event-by-event basis, since the RPS acceptance depends on both t and ξ. For each event, the raw values of ξ and t are obtained from the RPS tracker and used to fill the bins of a histogram. The value entered into the histogram is reduced by the average backround of $N_{bg} \times \Delta t$ events, where $|\Delta t|$ is the width of the t-bin, and increased by a factor of $1/A(t,\xi)$, where $A(t,\xi)$ is the RPS acceptance obtained from simulation. The number of entered events is set to zero if found to be ≤ 0 after subtracting the background.

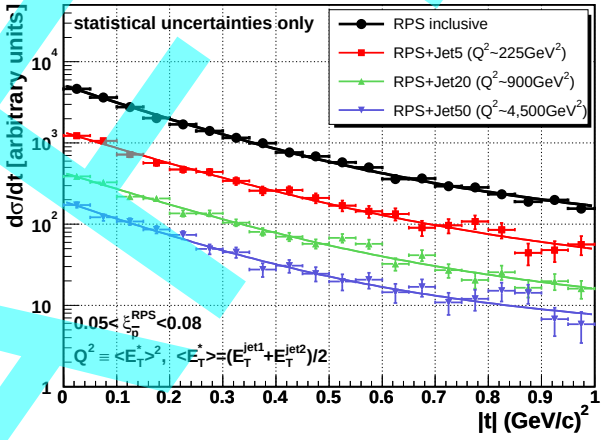


FIG. 20: **[make changes in inset]** The antiproton $|t|$ distribution for the SD⊕RPS$_{\rm track}$ data samples.

1. The b-slope at $t = 0$

Here we discuss the event selection requirements used for the measurement of the slope parameter at $t = 0$, the resulting slope, and the systematic uncertainties in the measurement.

Event selection. To minimize the effect of migration of events to and from adjacent ξ bins caused by resolution effects, events are selected in the region of $|t| \leq 1$ (GeV/c)^2 and $0.05 < \xi_{\bar{p}}^{\rm RPS} < 0.09$ where the RPS acceptance is approximately flat (see Fig. 7). To reject overlap backgrounds, these events are further required to be within $\xi_{\bar{p}}^{\rm CAL} < 0.1$ where the SD events dominate (see Fig. 6). The same expression that was used in the RPS dynamic allignment in Sec. V A, composed of two exponential terms with slopes b_1 and b_2 (Eq. 7), was used to fit the data and obtain the values of the slopes. Fits to data with only statististical uncertainties are shown in Fig. 20 for different $Q^{@}$ ranges. Systematic uncertainties are discussed below.

***b*-slope.** Results for the slope parameters b_1 and b_2 and for the ratios $b_1/b_1^{\rm incl}$ and $b_2/b_2^{\rm incl}$ are presented in Table V. The ratios $b_1/b_1^{\rm incl}$ are plotted in Fig. 21 with the ratio for the inclusive sample arbitrarily displayed at $Q^2 = 1$ (GeV/c)^2. No significant Q^2 dependence is observed over the entire range of 1 (GeV/c)^2 $< Q^2 <$ 10^4 (GeV/c)^2. The mean values of b_1 and b_2 over all data samples are 6.27 ± 0.30 (GeV/c)$^{-2}$ and 1.42 ± 0.11 (GeV/c)$^{-2}$, respectively. The measured slopes of the inclusive sample are in agreement with theoretical expectations [43].

Systematic uncertainties. We considered the dependence of the results on the RPS fiber tracker thresholds, the instantaneous luminosity, and the beam store and run number.

a. RPS fiber tracker thresholds Tracks in the RPS are reconstructed from hits above fiber threshold. A threshold value of 30 ADC counts is used for all three RPS stations. The slope values change by +1% (−1%) when the thereshold is lowered down to 20 (raised up to 35) ADC counts, which represent a decrease (increase) that doubles (reduces by 50%) the number of noise hits in the fiber tracker.

b. Instantaneous luminosity The RPS inclusive sample was divided into two sub-samples: one consisting of events collected at low instantaneous luminosities, $\mathcal{L} < 1.5 \cdot 10^{31}$cm^{-2}sec^{-1}, and the other of events collected at $\mathcal{L} > 3.5 \cdot 10^{31}$cm^{-2}sec^{-1}. A less than 2% difference between the slopes extracted from the two samples is observed, which is well within the statistical uncertainty.

c. Beam store/run number Variations in beam conditions with beam store and segments within a store may

DRAFT

BLESS

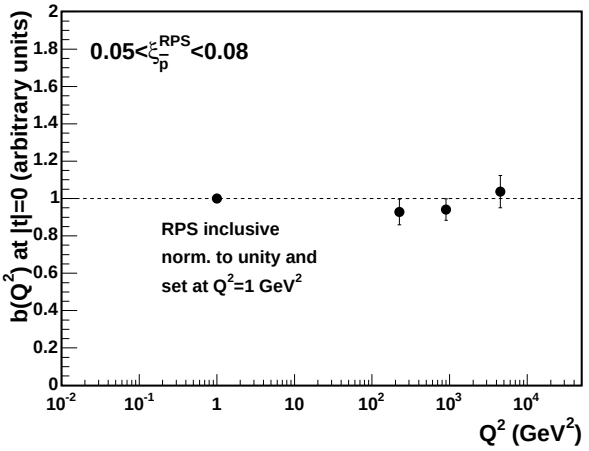


FIG. 21: The slope parameter b_1 of a fit to the form $d\sigma/dt = N \cdot (A_1 \cdot e^{b_1 \cdot t} + A_2 \cdot e^{b_2 \cdot t})$, with $A_2/A_1 = 0.11$ (see text), of SD events of different Q^2 values (from Table V) normalized to the slope of the RPS inclusive data sample, which is arbitrarily set at $Q^2 = 1$ GeV^2.

BLESS

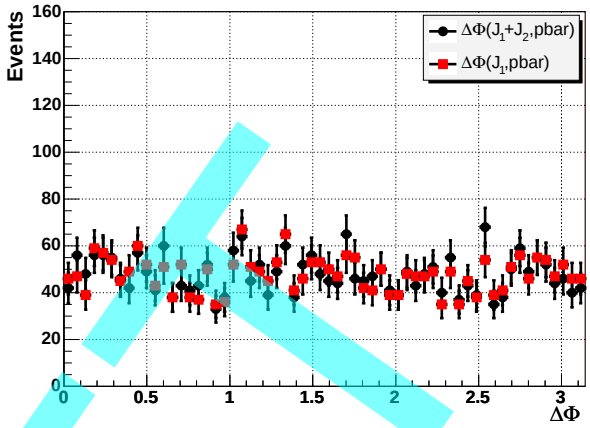


FIG. 22: [Vertical axis: **Events per $\Delta\phi = 0.05$**] Azimuthal angle difference between the outgoing antiproton and the average of the angles of the two leading jets, $\Delta\phi(J_1 + J_2, \text{pbar})$ (circles), or the angle of the leading jet, $\Delta\phi(J_1, \text{pbar})$ (squares), for SD events of the SD⊕RPS$_{\text{track}}$·Jet5 data sample. The error bars represent statistical uncertaintie.

affect the slope measurement. To estimate the uncertainty associated with varying beam conditions we measured the b-slopes of data sub-samples from different beam stores and different run numbers within a store. The values for b_1 and b_2 obtained were within the corresponding statistical uncertainties. A systematic uncertainty equal to the the statistical uncertainty was therefore assigned for this effect.

d. Dynamic alignment A systematic uncertainty of 5% was estimatred from the fits shown in Fig. 5 for the slope b_1 arising from the uncertanties of ± 60 μ in the (X, Y) position of the RPS detectors relative to the $\bar{p}$ beam.

The above systematic uncertainties are listed in Table VI.

TABLE VI: Systematic uncertainties in the slope parameters b_1 and b_2 (see Table V) of the diffractive t-distributions.

Source of uncertainty	δb_1	δb_2
RPS tracker threshold	1%	1%
Instantaneous luminosity	2%	2%
Beam store / run number	4%	8%
RPS alignment	5%	5%

BLESS

2. Azimuthal angle correlations

Using the SD⊕RPS$_{\text{track}}$·Jet5 data sample we have investigated correlations between the azimuthal angle of the outgoing antiproton and the dijet system. Two results have been obtained: one for the average of the angles of the two leading jets, $\Delta\phi(J_1 + J_2, \text{pbar})$ (circles), and the other for the angle of the leading jet, $\Delta\phi(J_1, \text{pbar})$ (squares). The $\Delta\phi$ distributions are plotted in Fig. 22. Both distributions are consistent with being flat within the statistical uncertainties.

3. Search for a diffraction minimum in the t-distribution

We searched for a diffraction minimum in the t-distribution using inclusive SD⊕RPS$_{\text{track}}$ and dijet SD⊕RPS$_{\text{track}}$·Jet5 data within $0.05 < \xi_{\bar{p}}^{RPS} < 0.08$. This ξ-range corresponds to a mean mass for the diffractively dissociated proton $\langle M_X \rangle > \approx \xi\sqrt{s} \approx 500$ GeV/c^2. The dijet data have $\langle Q^2 \rangle \approx 225$ (GeV/c)^2. The t-distributions are plotted in Fig. 19. As already discussed, the background in these data samples is $N_{bg} = 2/(\text{GeV/c})^2$, as estimated from the unphysical region of $|t| > |t_1| = 2.5$ (GeV/c)^2 for $Y_{\text{track}} > Y_0$.

Figure 23 shows distributions for the sum of both sides of the asymmetric distributions of Fig. 19 after background subtraction and acceptance corrections. The distributions are presented in a variable width histogram format. In filling up the histograms bins, a fraction is subtracted from each entry into a bin which is equal to the average background fraction in that bin, and the acceptance correction is then applied based on the RPS-measured values of ξ and t. The curve shown in the figure represents the electromagnetic form factor squared [43], $F_1(t)^2$, normalized to the $t = 0$ value of the RPS inclusive data in the region of $|t| < 0.5$ (GeV/c)^2. The $F_1(t)$ form factor used is given by [43]

DRAFT

$$F_1(t) = \frac{4m_p^2 - 2.8t}{4m_p^2 - t} \cdot \left(\frac{1}{(1 - t/0.71)}\right)^2, \qquad (12)$$

and in SD it enters in the form [43]

$$\frac{d\sigma^{SD}}{dt} = N_{norm} \cdot F_1(t)^2 \cdot \exp\left[2\alpha' \cdot \ln\frac{1}{\xi} \cdot t\right], \qquad (13)$$

where α' is the slope of the the Pomeron trajectory. In the range of $|t| < 1$ (GeV/c)^2 and $0.05 < \xi < 0.08$ the two-component exponential form of Eq. (7) with $A_2/A_1 = 0.11$ which was used in the dymamic alignment method is a good approximation to that of Eq. (13) with $\langle\xi\rangle = 0.065$ substituted for ξ.

The following features of the t-distributions are notable:

- *low-t region ($|t| \lesssim 0.5$ (GeV/c)^2):* the RPS data are in good agreement with the DL curve;
- *scale independence:* the distributions of the RPS and RPS·Jet5 data are similar in shape;
- *high-$|t|$ region ($|t| \gtrapprox 0.5$ (GeV/c)^2):* the RPS data lie increasingly higher than the DL curve as $|t|$ increases, becoming approximately flat for $|t| \gtrsim 2$ (GeV/c)^2 with a hint of a broad minimum at $|t| \sim 2.5$ (GeV/c)^2.

BLESS

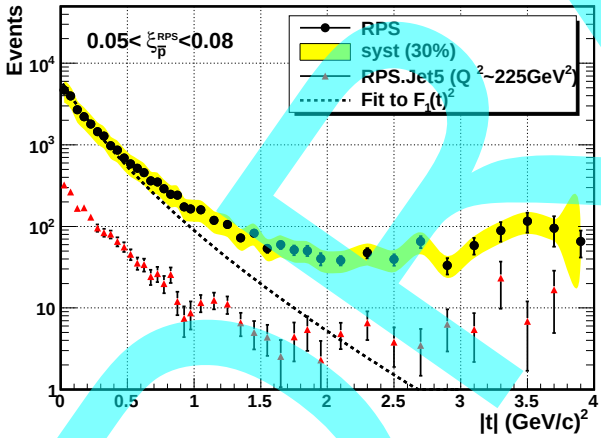


FIG. 23: [Change "Events" on vertical axis to "Events per $\Delta|t|$ bin width and change "Fit to..." in the inset to "DL"] t-distributions corrected for RPS acceptance after background subtraction: (*circles*) RPS [SD⊕RPS$_{\rm track}$] data; (*triangles*) RPS·Jet5 [SD⊕RPS$_{\rm track}$·Jet5] data of $\langle Q^2\rangle \simeq 225$ (GeV/c)^2. The curve labeled DL arepresents the distribution expected for soft SD in the Donnachie-Landshoff model [43] (Eq. 13) normalized to the RPS data within $|t| \lesssim 0.5$ (GeV/c)^2.

The physics significance of these results are briefly discussed below.

a. Low-t region The good agreement between the inclusive t-distribution and the DL prediction in this region serves as a pedestal for our search for deviations in the region of $|t| \gtrsim 0.5$ (GeV/c)^2 that could arise from a diffraction minimum.

b. scale independence The scale independence of the distributions points to a factorization property between the exchange that produces the recoiling $\bar{p}$ and the associated rapidity gap on one hand, and the final state into which the proton dissociates on the other. Such behavior favors models in which the hard scattering is controlled by the low–x parton distribution function of the recoiling antiproton, just as in ND interactions, while a color-neutral soft exchange allows the antiproton to escape intact forming the rapidity gap (see, e.g., Refs. [44]-[47]).

c. High-t region A minimum ("dip") in the t-distribution could occur as a result of destructive interference between the real and imaginary parts of the scattering amplitude. Diffractive minimums in elastic scattering have been previously reported, and the position of the minimum has been found to depend on $\sqrt{s}$, decreasing with increasing $\sqrt{s}$ (see, e.g., Ref. [48]). Recently, the D0 collaboration reported a preliminary Tevatron Run II result on elastic $\bar{p}p$ scattering at $\sqrt{s} = 1960$ GeV, in which a minimum (broadened by resolution effects) is observed at $|t| \sim 0.7$ (GeV/c)^2 followed by a maximum ("bump") at $|t| \sim 1$ (GeV/c)^2 [49].

A minimum in a diffractive t-distribution has never been previously reported. Since the quasi-elastic diffractive scattering occurs at $s' = \xi s < s$, a diffractive minimum would be expected to lie at a higher $|t|$ than in elastic scattering and have a width broadened by the effects of the size of the bin $\Delta\xi$ and of the t resolution.

The expected contributions to the width of a diffractive dip are summarized below:

(a) ξ-bin width: from Eq. (13), $\Delta|t|_{\xi-\rm bin} = \Delta\ln(1/\xi) = \ln(1/0.05) - \ln(1/0.08) = 0.47$;

(b) $\delta\xi$ and δt resolutions: from Refs. [10, 14], $\delta\xi = 0.001$ and $\delta t = \pm 0.07$ (GeV/c)^2 for $\langle|t|\rangle \approx 0.05$ (GeV/c)^2 with a dependence $\propto \sqrt{|t|}$, resulting for $|t| \approx 2.5$ (GeV/c)^2 in a value larger by a factor $\sqrt{2.5}/\sqrt{0.05} \approx 7$ that yields $\delta t_{\rm res} \approx 0.5$;

(c) total width expected : $\Delta t_{|t|=2.5} = \Delta|t|_{\xi-\rm bin} + \delta t_{\rm res} \approx 1$ (GeV/c)^2, where the contributions have been added linearly since the ξ-bin width simply is not a random variable.

The data plotted presented in Fig. 23 are consistent with the above analysis and thus represent the first observation of a diffraction minimum in a $\bar{p}p$ collisions.

VII. CONCLUSION

Results are presented from a measurement of diffractive dijet production in $\bar{p}p$ collisions at $\sqrt{s} = 1.96$ TeV,

$p + \bar{p} \to \bar{[}jet1 + jet2 + X] + \bar{p}$, extracted from data collected in Run II of the Fermilab Tevatron $\bar{p}p$ Collider using the CDF II detector. A system of special forward detectors including a roman pot spectrometer for measuring the momentum of the outgoing $\bar{p}$ were used. The measured diffractive dijet production rates as a function of $x_{Bj}^{\bar{p}}$ ($x^{\bar{p}}$-Bjorken), $Q^2 \approx \langle E_T \rangle^2$, $\xi_{\bar{p}}$ and $t_{\bar{p}}$ are compared with the corresponding non-diffractive rates at the same $x_{Bj}^{\bar{p}}$ and Q^2. The physics interest in these measurements is to elucidate the QCD nature of the diffractive exchange, traditionally referred to as *Pomeron*.

Our results are extracted from data samples of diffractive and non-diffractive events corresponding to 310 pb^{-1} of integrated luminosity. To reduce systematic uncertainties, the diffractive and non-diffractive data were collected simultaneously using the same calorimeter trigger to accept high-E_T jets, and were similarly analyzed. The measurements cover the region of $0.03 < \xi_{\bar{p}} < 0.09$, $|t_{\bar{p}}| \leq 4$ (GeV/c)^2, $0.001 < x_{Bj}^{\bar{p}} < 0.09$ and 10^2 (GeV/c)$^2 < Q^2 < 10^4$ (GeV/c)^2.

The $E_T^{\rm jet}$ distribution shapes are similar for SD and ND events, and the $x_{Bj}^{\bar{p}}$ distribution of the ratio of SD/ND production rates is relatively flat in the region of $\beta \equiv x/\xi \leq 0.5$, where β is the fractin of the momentum loss carried by the parton in the Pomeron that participates in the interaction. A fit of the form $\mathcal{R} = \mathcal{R}_\circ \cdot x_{Bj}^r$ in the region of $0.001 < x_{Bj}^{\bar{p}} < 0.025$, where $\beta < 0.5$, yields $r = -0.44 \pm 0.04$ and $\mathcal{R}_\circ = (8.6 \pm 0.8) \times 10^{-3}$, consistent with the Run I CDF result of $r = -0.45 \pm 0.02$ and $\mathcal{R}_\circ = (6.1 \pm 0.1) \times 10^{-3}$ within the normalization systematic uncertainty of $\pm 30\%$ common to the Run I and Run II data samples.

The Q^2 dependence of the ratio of SD/ND rates is relatively weak, varying by less than a factor of ~ 2 over the measured Q^2 range within which the individual SD and ND distributions vary by a factor of $\sim 10^4$ as observed in the E_T^* dependence of the differential cross sections.

The t-distributions for $|t| < 1$ (GeV/c)^2 can be fitted with a sum of two exponential terms of the form $d\sigma/dt = N \cdot \left(A_1 \cdot e^{b_1 \cdot t} + A_2 \cdot e^{b_2 \cdot t}\right)$. The slope parameters b_1 and b_2 are found to be independent of Q^2 over the range of ~ 1 (GeV/c)$^2 < Q^2 < 10^4$ (GeV/c)^2. The mean values of b_1 and b_2 are 6.27 ± 0.30 (GeV/c)$^{-2}$ and 1.42 ± 0.11 (GeV/c)$^{-2}$, respectively. The measured slopes of the inclusive sample are in agreement with theoretical expectations [43].

A search for a diffraction minimum in the t-distribution was conducted using data with $0.05 < \xi_{\bar{p}}^{\rm RPS} < 0.08$ and $|t|$ up to 4 (GeV/c)^2. Two event samples were studied, an inclusive sample and a dijet sample of $\langle Q^2 \rangle \approx 225$ (GeV/c)^2. The distributions for both samples are substantially flatter than the expectation from the electromagnetic form factor of the proton, Eq. (13), consistent with a diffraction minimum at $|t| \sim 2.5$ (GeV/c)^2 filled by t-resolution and ξ-dispersion effects. At $|t| \sim 3$ (GeV/c)^2, the measured cross section for the inclusive event sample is a factor of ~ 10 larger than the value predicted by the proton electromagnetic form factor normalized to the data distribution in the region of $|t| < 0.5$ (GeV/c)^2.

The relatively flat $x_{Bj}^{\bar{p}}$ distribution and the small Q^2 dependence of the diffractive to non-diffractive ratios, combined with the Q^2 independence of the t-distributions, favor models of hard diffractive production in which the hard scattering is controlled by the parton distribution function of the recoil antiproton while the rapidity gap formation is governed by a color-neutral soft exchange [44]-[47].

Acknowledgments

We thank the Fermilab staff and the technical staffs of the participating institutions for their vital contributions. This work was supported by the U.S. Department of Energy and National Science Foundation; the Italian Istituto Nazionale di Fisica Nucleare; the Ministry of Education, Culture, Sports, Science and Technology of Japan; the Natural Sciences and Engineering Research Council of Canada; the National Science Council of the Republic of China; the Swiss National Science Foundation; the A.P. Sloan Foundation; the Bundesministerium für Bildung und Forschung, Germany; the Korean Science and Engineering Foundation and the Korean Research Foundation; the Particle Physics and Astronomy Research Council and the Royal Society, UK; the Institut National de Physique Nucleaire et Physique des Particules/CNRS; the Russian Foundation for Basic Research; the Comisión Interministerial de Ciencia y Tecnología, Spain; the European Community's Human Potential Programme under contract HPRN-CT-2002-00292; and the Academy of Finland.

DRAFT

[1] F. Abe et al. (CDF Collaboration), "Measurement of small angle antiproton-proton elastic scattering at $\sqrt{s} =$ 546 and 1800 GeV," Phys. Rev. D **50**, 5518-5535 (1994).

[2] F. Abe et al. (CDF Collaboration), "Measurement of the antiproton-proton total cross section at sqrt(s) =546 and 1800 GeV," Phys. Rev. **50**, 5550-5561 (1994).

[3] F. Abe et al. (CDF Collaboration), "Measurement of $\bar{p}p$ single diffraction dissociation at $\sqrt{s} = 546$ and 1800 GeV," Phys. Rev D **50**, 5535 (1994).

[4] F. Abe et al., (CDF Collaboration), "Observation of rapidity gaps in $\bar{p}p$ collisions at 1.8 TeV," Phys. Rev. Lett. **74**, 855-859 (1995).

[5] F. Abe et al. (CDF Collaboration), "Observation of Diffractive W-Boson Production at the Fermilab Tevatron,"' Phys. Rev. Lett. **78**, 2698-2703 (1997).

[6] F. Abe et al. (CDF Collaboration), "Measurement of

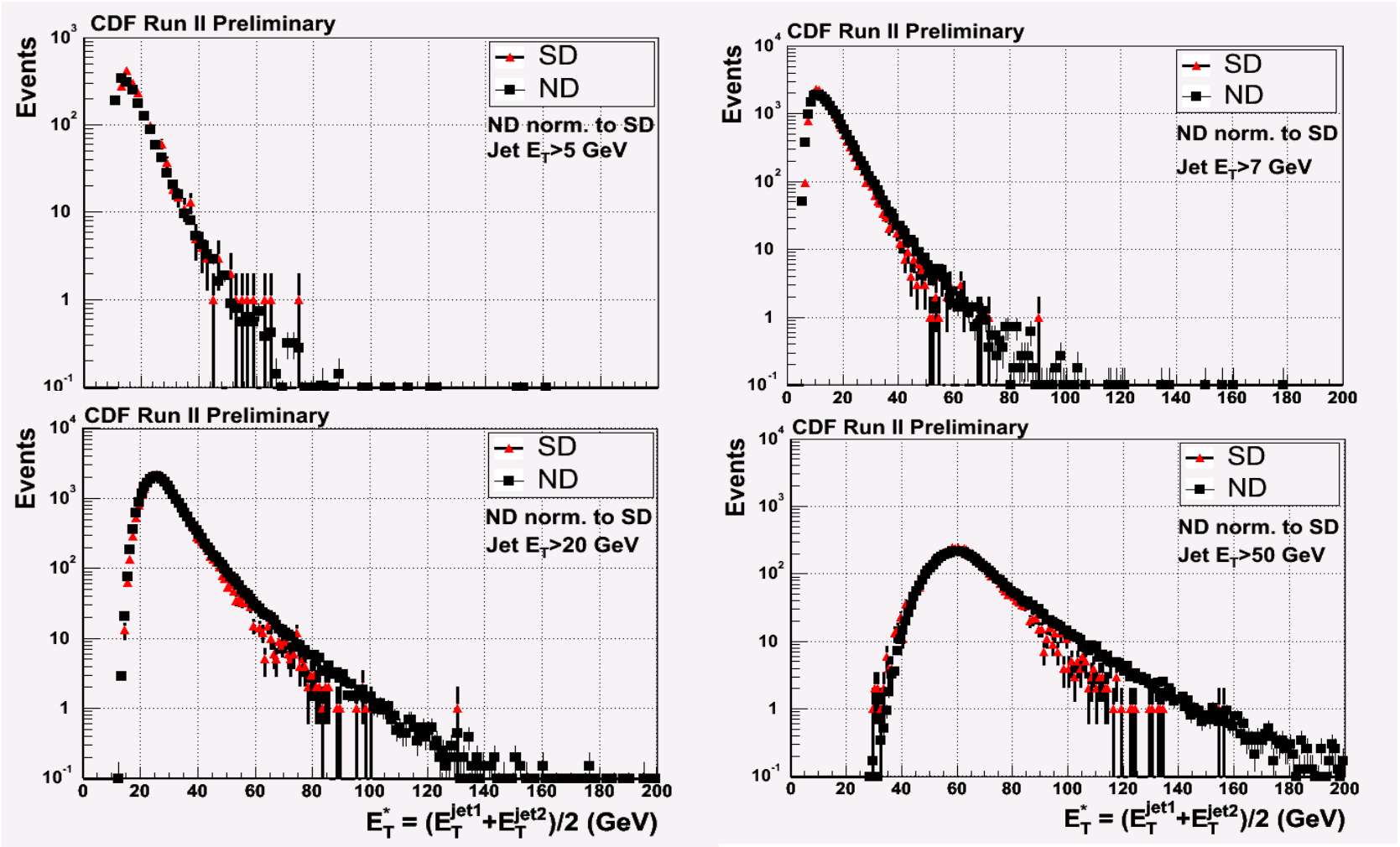
Diffractive Dijet Production at the Fermilab Tevatron," Phys. Rev. Lett. **79**, 2636-2641 (1997).
[7] F. Abe et al. (CDF Collaboration), 'Dijet Production by Color-Singlet Exchange at the Fermilab Tevatron," Phys. Rev. Lett. **80**, 1156-1161 (1998).
[8] F. Abe et al., (CDF Collaboration)," Events with a Rapidity Gap between Jets in $\bar{p}p$ Collisions at sqrt(s)=630 GeV," Phys. Rev. Lett. **81**, 5278-5283 (1998).
[9] T. Affolder et al. (CDF Collaboration), "Observation of Diffractive b-Quark Production at the Fermilab Tevatron," Phys. Rev. Lett. **84**, 232-237 (2000).
[10] T. Affolder et al. (CDF Collaboration), "Diffractive Dijets with a Leading Antiproton in pbar-p Collisions at sqrt(s)=1800 GeV," Phys. Rev. Lett. **84**, 5043-5048 (2000).
[11] T. Affolder et al. (CDF C0llaboration), "Dijet Production by Double Pomeron Exchange at the Fermilab Tevatron," Phys. Rev. Lett. **85**, 4215-4220 (2000).
[12] T. Affolder et al. (CDF Collaboration), "Double Diffraction Dissociation at the Fermilab Tevatron Collider," Phys. Rev. Lett. **87**, 141802-(1-6) (2001).
[13] T. Affolder et al. (CDF Collaboration), "Observation of Diffractive J/ψ Production at the Fermilab Tevatron," Phys. Rev. Lett. **87**, 241802-(1-6) (2001).
[14] D. Acosta et al. (CDF Collaboration), "Diffractive Dijet Production at sqrt(s)=630 and 1800 GeV at the Fermilab Tevatron," Phys. Rev. Lett. **88**, 151802-(1-6) (2002).
[15] D. Acosta et al. (CDF collaboration), "Central pseudorapidity gaps in events with a leading antiproton at the Fermilab Tevatron $\bar{p}p$ Collider," Phys. Rev. Lett. **91**, 011802-(1-6) (2003).
[16] D. Acosta et al. (CDF collaboration), "Inclusive Double-Pomeron Exchange at the Fermilab Tevatron pbar-p Collider," Phys. Rev. Lett. **93**, 141601-(1-7) (2004).
[17] T. Aaltonen et al. (CDF Collaboration), " Search for exclusive gamma gamma production in hadron-hadron collisions," Phys. Rev. Lett. **99**, 242002 (2007).
[18] T. Aaltonen et al. (CDF Collaboration), "Observation of Exclusive Dijet Production at the Fermilab Tevatron $p\bar{p}$ Collider," Phys. Rev. D **77**, 052004 (2008).
[19] Rapidity, $y = \frac{1}{2}\ln\frac{E+p_L}{E-p_L}$, and pseudorapidity, $\eta = -\ln\tan\frac{\theta}{2}$, are used interchangeably, since in the kinematic region of interest they are approximately equal.
[20] The rapidity gap width, Δy, and the forward momentum loss fraction, ξ, are kinematically related by $\Delta y = -\ln\xi$.
[21] P. D. B. Collins, *An Introduction to Regge Theory and High Energy Physics*, Cambridge University Press, Cambridge, (1977).
[22] V. Barone and E. Predazzi, *High-Energy Particle Diffraction*, Springer Press, Berlin, (2002).
[23] S. Donnachie, G. Dosch, P. Landshoff, and O. Nachtmann, *Pomeron Physics and QCD*, Cambridge University Press, Cambridge, (2002).
[24] K. Goulianos, "Hadronic diffraction: where do we stand"? in *Les Rencontres de Physique de la Vallee d'Aoste: Results and Perspectives in Particle Physics, La Thuile, Italy, February 27 - March 6, 2004*, Frascati Physics Series, Special 34 Issue, edited by Mario Greco; arXiv:hep-ph/0407035.
[25] The diffracted (leading) nucleon is assumed to be the antiproton, which at CDF can be detected in a Roman Pot Spectrometer (RPS) installed along the outgoing $\bar{p}$ direction (there is no RPS on the p side).
[26] F. Abe *et al.* (CDF Collaboration), "Topology of three-jet events in $\bar{p}p$ collisions at $\sqrt{s}$ =1.8 TeV," Phys. Rev. D **45**, 1448 (1992).
[27] K. Hatakeyama, "Measurement of the Diffractive Structure Function of the Antiproton in Proton-Antiproton Collisions at $\sqrt{s} = 1800$ and 630 GeV," Ph.D. thesis, The Rockefeller University, 2003 (fermilab-thesis-2003-18).
[28] M.G. Albrow *et al.* (CDF Collaboration), "Further Studies in Hard Diffraction and Very Forward Physics", fermilab-proposal-0916, Oct 1999; `http://lss.fnal.gov/archive/test-proposal/0000/fermilab-proposal-0916.shtml`.
[29] K. Goulianos, M. Gallinaro, K. Hatakeyama, S. Lami, C. Mesropian, A. Solodsky, "The CDF Miniplug Calorimeters," Nucl. Instrum. Methods A **496**, 333 (2003).
[30] Michele Gallinaro for the CDF Collaboration, "CDF Forward Detectors and diffractive structure functions at the Fermilab Tevatron," Proceedings of the 9th Hadron Physics and 8th Relativistic Aspects of Nuclear Physics (HADRON-RANP 2004), Angra dos Reis, Rio de Janeiro, Brazil, March 28-April 3, 2004; FERMILAB-CONF-04-308-E, hep-ph/0407255.
[31] D. Acosta *et al.*, Nucl. Instrum. Methods A **494**, 57 (2002).
[32] F. Abe *et al.* (CDF Collaboration), Nucl. Instrum. Methods A **271**, 387 (1988);
[33] D. Acosta *et al.* (CDF Collaboration), Phys. Rev. D **71**, 032001 (2005).
[34] A. Sill *et al.*, Nucl. Instrum. Methods A **447**, 1 (2000).
[35] A. Affolder *et al.*, Nucl. Instrum. Methods A **526**, 249 (2004).
[36] L. Balka *et al.*, Nucl. Instrum. Methods A **267**, 272 (1988).
[37] S. Bertolucci *et al.*, Nucl. Instrum. Methods A **267**, 301 (1988).
[38] M. Albrow *et al.*, Nucl. Instrum. Methods A **480**, 524 (2002).
[39] Konstantin Goulianos and Stefano Lami, *Performance of a Prototype Position Sensitive Towerless Calorimeter,* Nucl. Instrum. Methods A **430**, 34-47 (1998).
[40] G.C. Blazey *et al.*, *"Run II Jet Physics: Proceedings of the Run II QCD and Weak Boson Physics Workshop"*; ArXiv:hep-ex/0005012.
[41] Transverse energy is defined as $E_T = E\sin\theta$, and missing E_T as $\not\!\!E_T = |\overrightarrow{\not\!\!E_T}|$ with $\overrightarrow{\not\!\!E_T} = -\sum_i E_T^i \hat{n}_i$, where $\hat{n}_i$ is a unit vector perpendicular to the beam axis and pointing at the i^{th} calorimeter tower. The sum E_T is defined by $\sum E_T = \sum_i E_T^i$. Both sums are over all calorimeter towers above the set thresholds. The missing E_T significance is defined as $S_{\not\!\!E} \equiv \not\!\!E_T/\sqrt{\Sigma E_T^2}$
[42] Konstantin Goulisnos, Diffraction at CDF, in Proc. *12^{th} International Conference on Elastic and Diffractive Scattering - Forward Physics and QCD (EDS07)*, DESY, Hamburg, Germany 21-25 May 2007; `http://www.desy.de/~eds07/proceedings.html`.
[43] A. Donnachie and P. Landshoff, "New data and the hard Pomeron," Phys. Lett. B **518** (2001) 63, hep-ph/0105088, and references therein.
[44] Konstantin Goulianos, "Renormalized Diffractive Parton Densities," PoS (DIFF2006) 044 (and references therein), Presentad at *Diffraction 06, International Workshop on Diffraction in High-Energy Physics* September 5-10, 2006, Adamantas, Milos island, Greece.

DRAFT

[45] Stanley J. Brodsky, Rikard Enberg, Paul Hoyer, and Gunnar Ingelman4,"Hard diffraction from parton rescattering in QCD," Phys. Rev. D **71**, 074020 (2005).
[46] A. B. Kaidalov, V. A. Khoze, A. D. Martin, and M. G. Ryskin, "Probabilities of rapidity gaps in high energy interactions," Eur. Phys. J. C **21** (2001) 521; [arXiv:hep-ph/0105145].
[47] B.Z. Kopeliovich, I.K. Potashnikova, I. Schmidt, and A.V. Tarasov, "Diffractive Excitation of Heavy Flavors: Leading Twist Mechanisms," arXiv:hep-ph/0702106v2.
[48] M. M. Islam, R .J .Luddy, A. V. Prokudin, "*pp* elastic scattering at LHC in near foirward direction," Phys. Lett. B **605** (2005) 115-122.
[49] D0 preliminary result on elasic scattering.

DRAFT

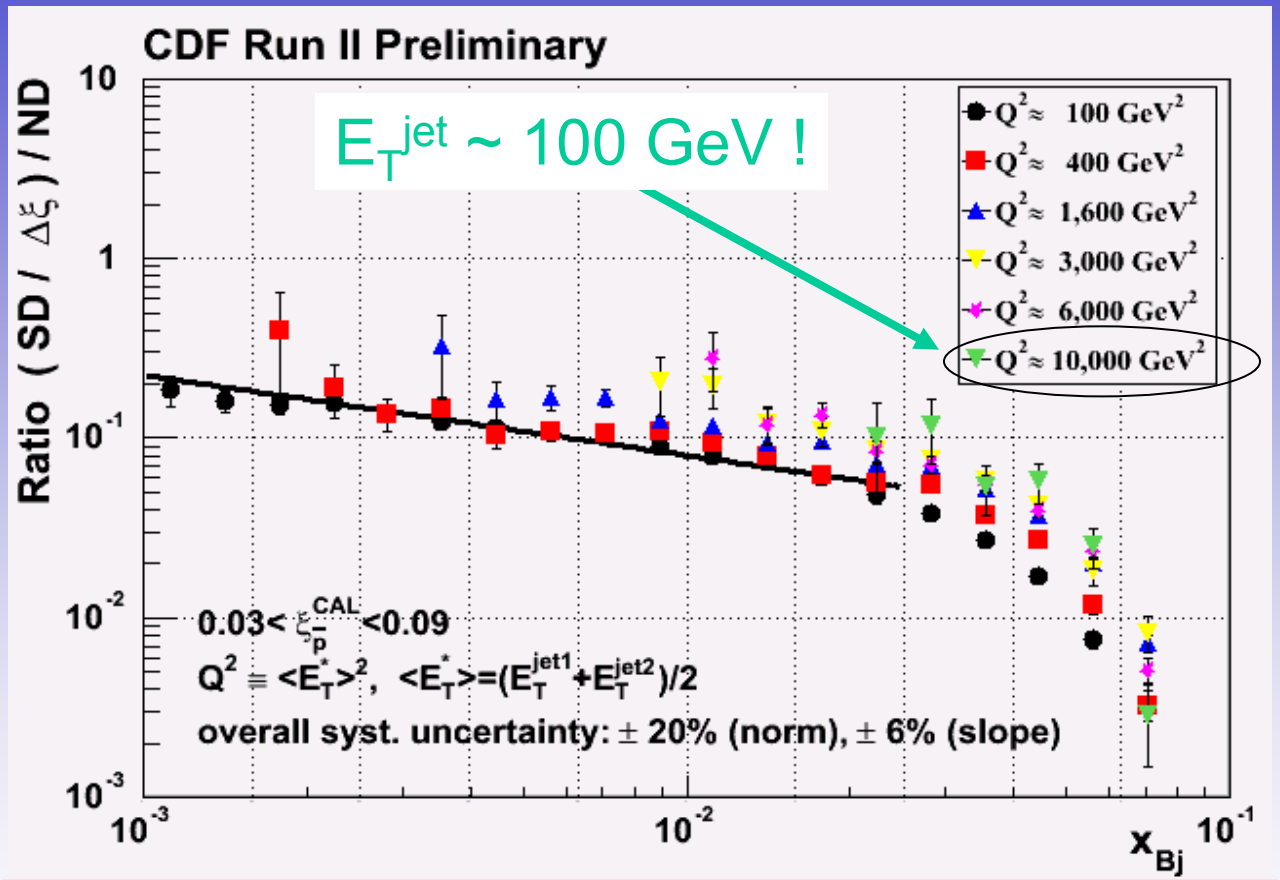
Dijets - E_T distributions



➔ similar for SD and ND over 4 orders of magnitude

Kinematics

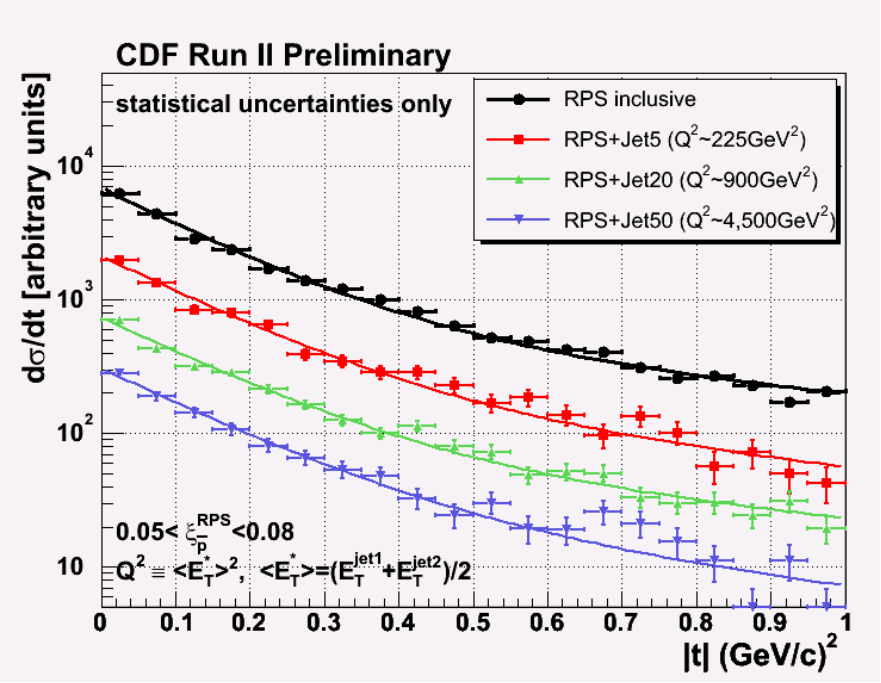
Dijet DSF: x_{Bj} and Q^2 dependence

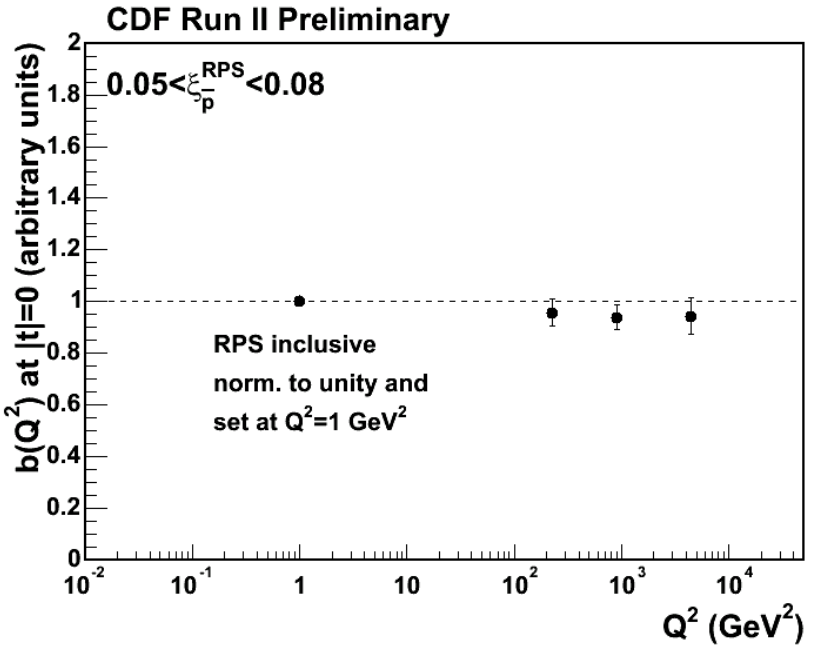


Small Q^2 dependence in region $100 < Q^2 < 10{,}000$ GeV^2

⇨ Pomeron evolves as the proton!

Dijets - diffractive structure function
t- dependence





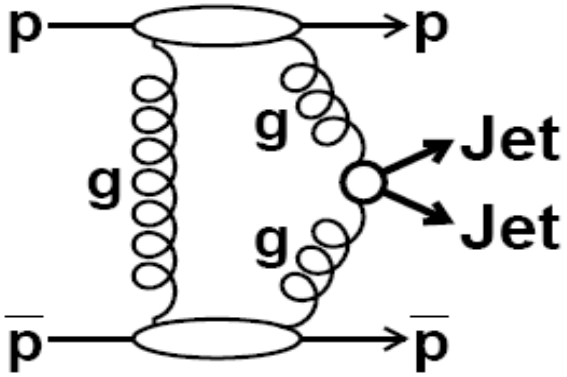
Fit dσ/dt to a double exponential

$$F = 0.9 \cdot e^{b_1 \cdot t} + 0.1 \cdot e^{b_2 \cdot t}$$

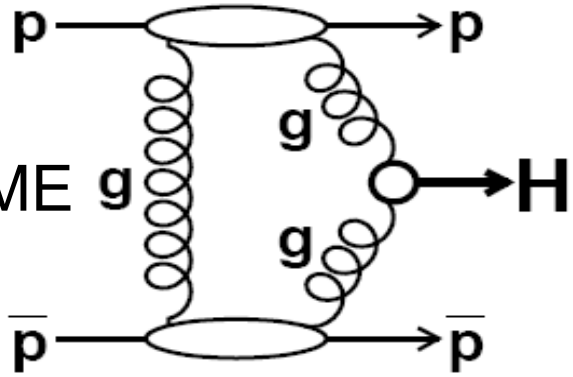
- No Q2 dependence in slope from inclusive to $Q^2 \sim 10^4$ GeV^2
- Same slope over entire region of $\sim 1 < Q^2 < 4{,}500$ GeV^2

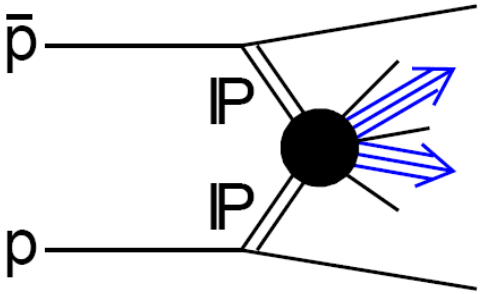
Exclusive Dijet and Higgs Production

Phys. Rev. D 77, 052004

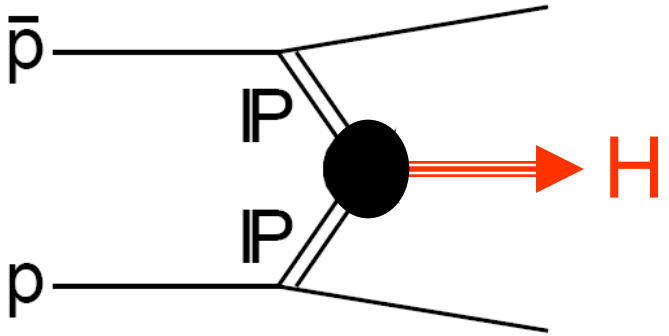


ExHuME

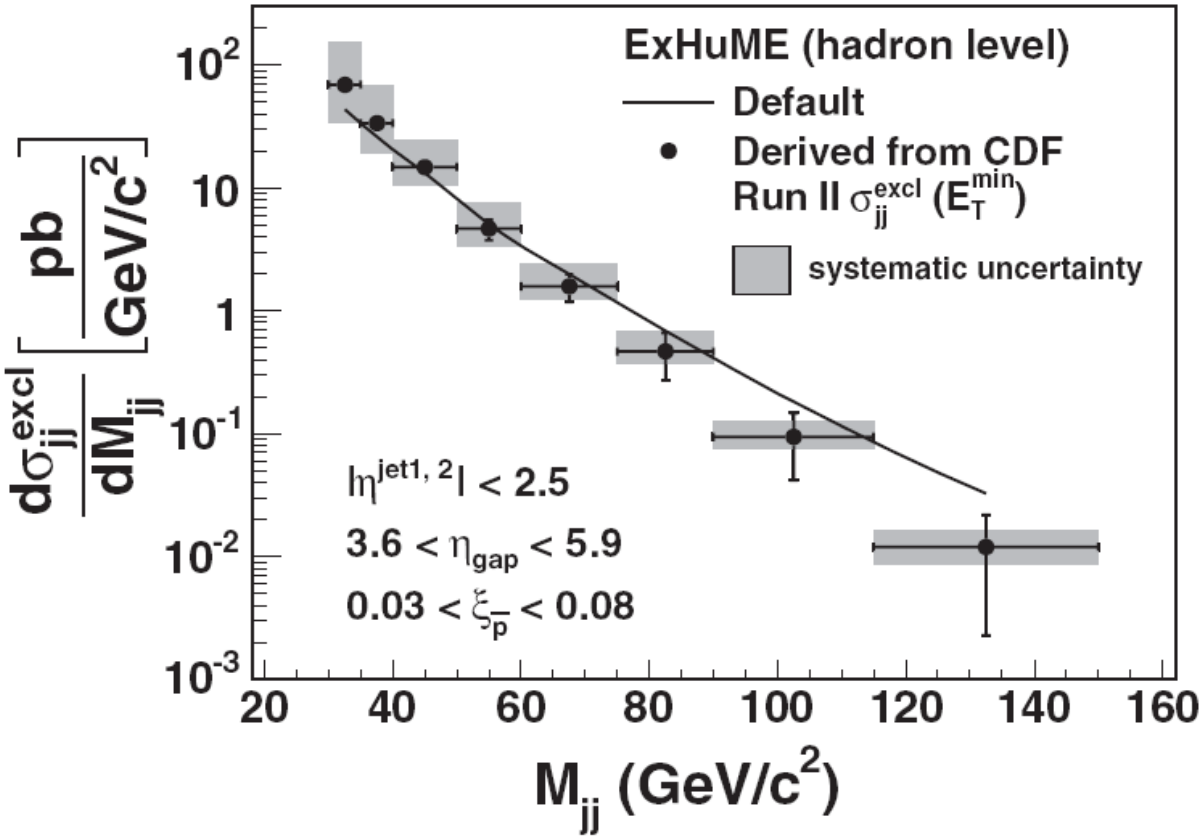




DPEMC



Exclusive Dijet x-section vs. M_{jj}



line: ExHuME hadron-level exclusive di-jet cross section vs. di-jet mass
points: derived from CDF excl. di-jet x-sections using ExHuME

Stat. and syst. errors are propagated from measured cross section uncertainties using M_{jj} distribution shapes of ExHuME generated data.

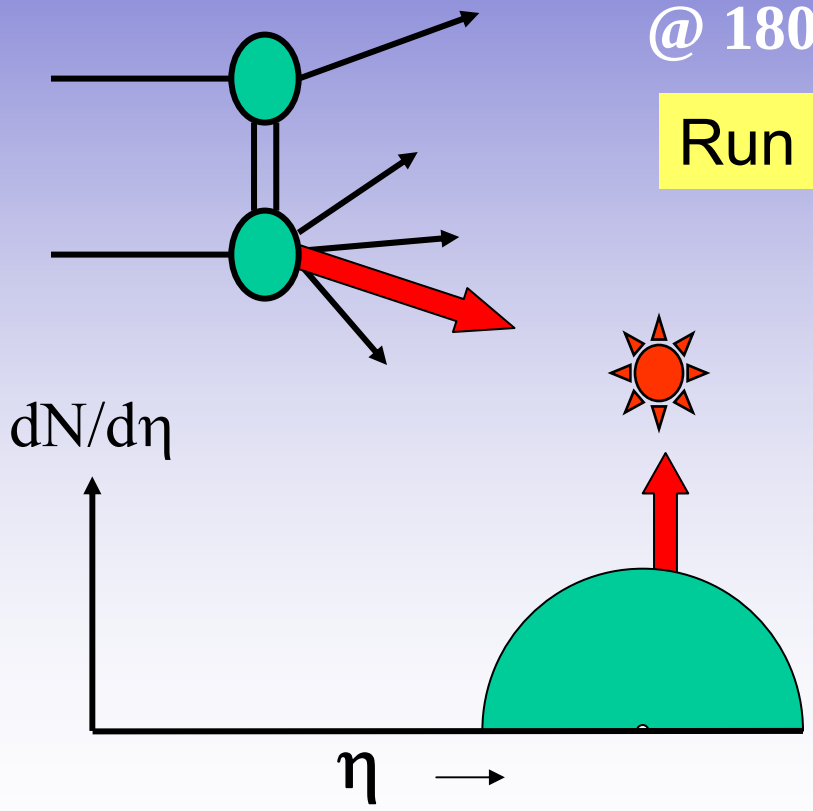
Hard diffractive fractions

$$\bar{p}p \rightarrow (\odot + X) + \text{gap}$$

Fraction: SD/ND @ 1800 GeV

Run I

⊙	Fraction (%)
JJ	0.75 +/- 0.10
W	0.115 +/- 0.55
b	0.62 +/- 0.25
J/ψ	1.45 +/- 0.25



All fractions ~ 1%
(differences due to kinematics)

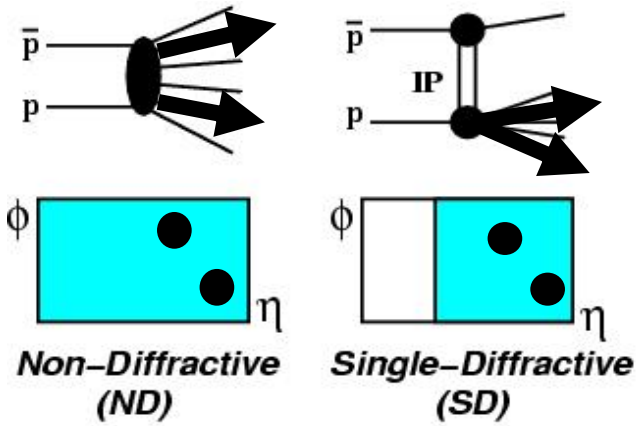
- ~ uniform suppression
- ~ FACTORIZATION !

Diffraction at CDF: ongoing analyses

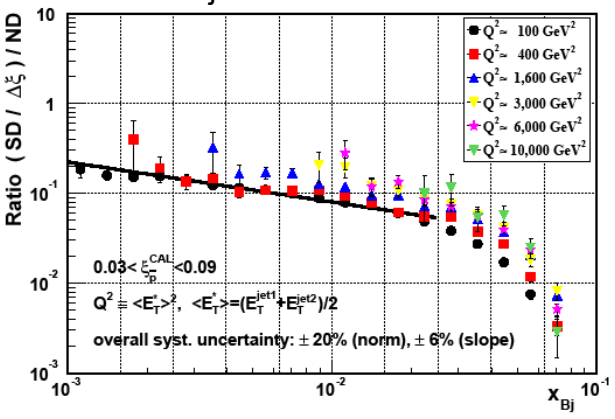
Diffractive dijets……	Gallinaro	under internal review
DSF in DPE……	Terashi	final stages of analysis
Diffractive W/Z……	Convery	under internal review
Central gaps……	Mesropian	towards internal review

DSF from Dijets in Run II

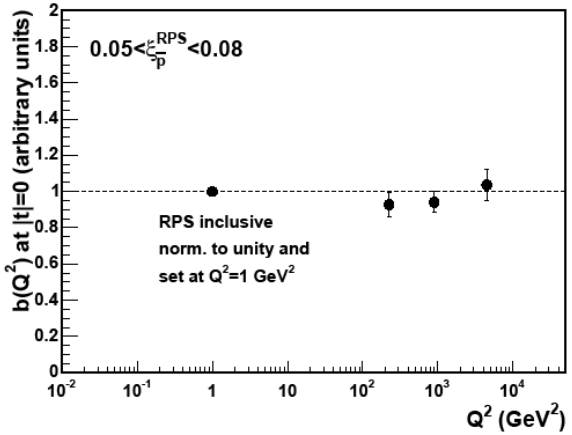
$$R(x_{Bj}) \equiv \frac{Rate_{jj}^{SD}(x_{Bj})}{Rate_{jj}^{ND}(x_{Bj})} \Rightarrow \frac{F_{jj}^{SD}(x_{Bj})}{F_{jj}^{ND}(x_{Bj})}$$



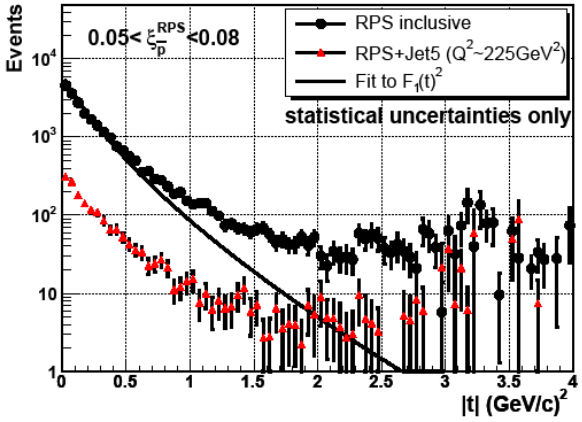
x_{Bj} - distribution



b - slope of t-distribution



t - distribution

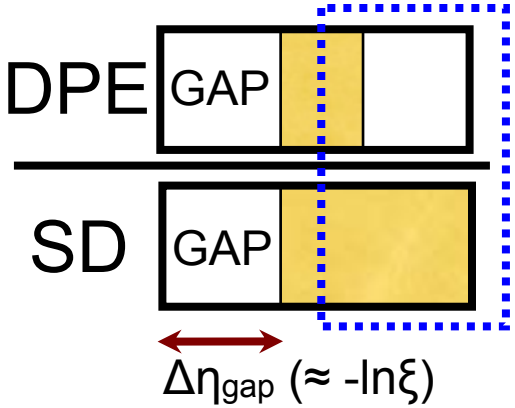


- The x_{Bj}-distribution of the SD/ND ratio has no strong Q^2 dependence
- the slope of the t-distribution is independent of Q^2
- the t-distribution displays a diffraction minimum at $|t| \sim 2.5$ (GeV/c)^2 (?)

➢ all three results ➔ "first observation"

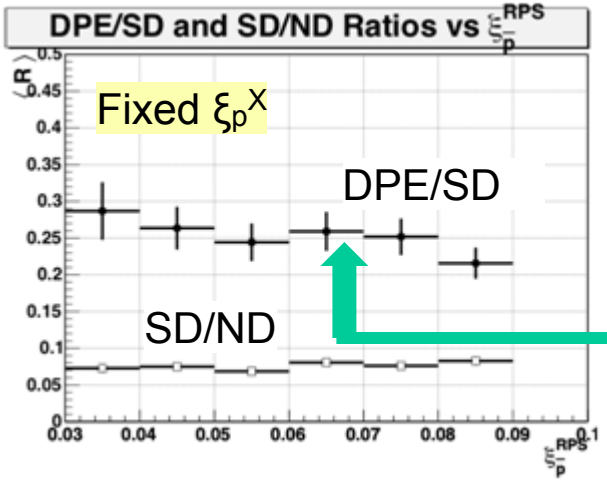
DSF from Dijets in DPE

QCD factorization holds for the formation of the 2nd gap



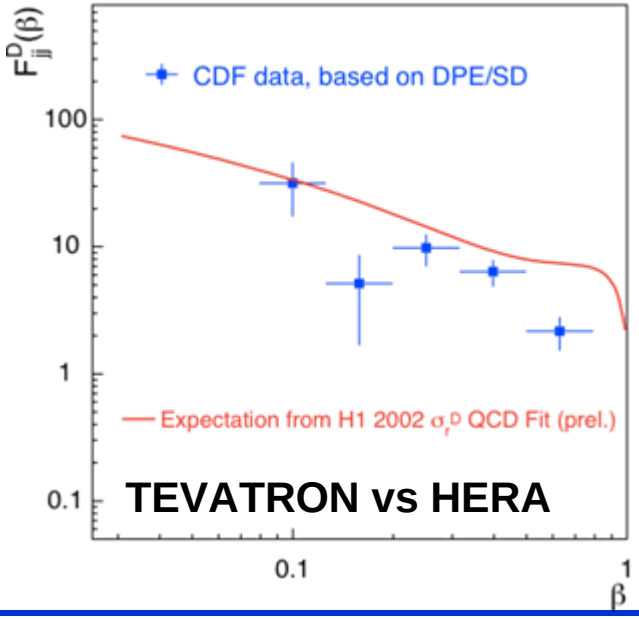
F_{jj}^{D}

ξ_{pbar}^{RPS} dependence

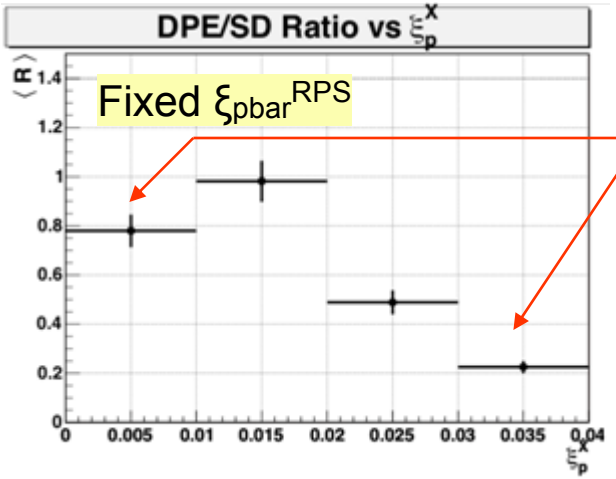


- $E_T^{Jet1,2}$>10 GeV
- 3.6<η_{gap}<5.9
- RP good track
- 0.01<ξ_{pbar}^{X}<0.12

factorization restored



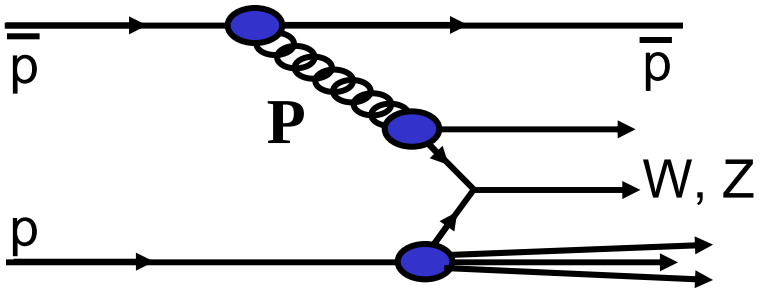
ξ_p^X dependence



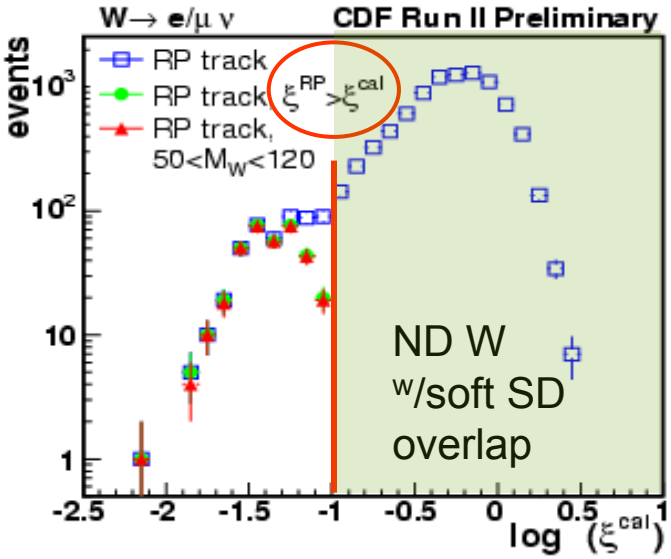
Ratio falls off at low and high ξ_p^X → kinematics

Diffractive W/Z Production

- probes the quak content of the Pomeron

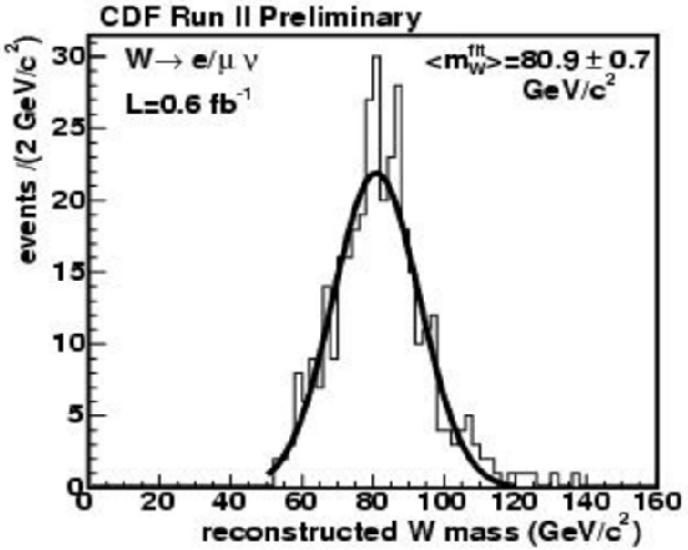


- use CAL and Roman pots to get η_ν



$$\xi^{cal} = \sum_{towers} \frac{E_T}{\sqrt{s}} e^{-\eta}$$

$$\xi^{RPS} - \xi^{cal} = \frac{\not{E}_T}{\sqrt{s}} e^{-\eta_\nu}$$



CDF (press release 2007): 80,413 +/- 48 MeV/c^2

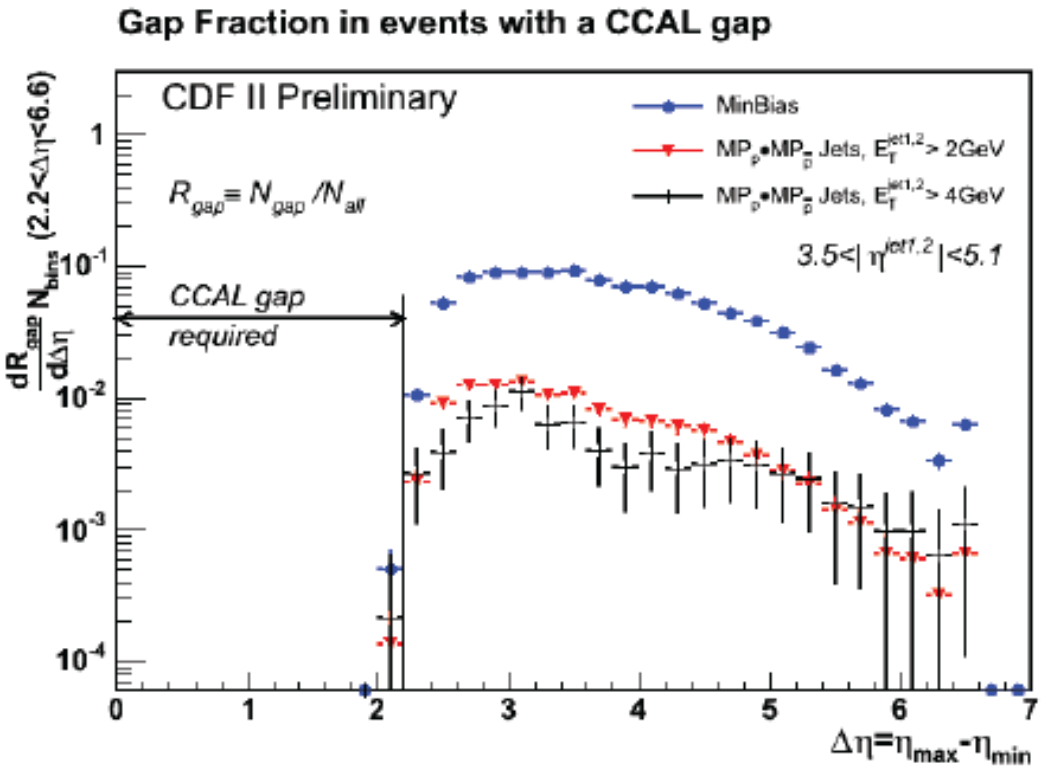
RESULTS

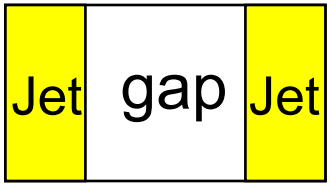
R^W (0.03 < ξ < 0.10, |t|<1)= [0.97 ± 0.05(stat) ± 0.11(syst)]%

Run I: R^W =1.15±0.55 % (ξ<0.1)➔ estimate **0.97±0.47 % (0.03 < ξ < 0.10 & |t|<1)**

R^Z (0.03 < ξ < 0.10, |t|<1)= [0.85 ± 0.20(stat) ± 0.11(syst)]%

Central gaps





The distribution of the gap fraction $R_{gap}=N_{gap}/N_{all}$ vs $\Delta\eta$ for MinBias ($CLC_p \bullet CLC_{pbar}$) and MiniPlug jet events ($MP_p \bullet MP_{pbar}$) of $E_{T(jet1,2)}>2$ GeV and $E_{T(jet1,2)}>4$ GeV.

The distributions are similar in shape within the uncertainties.

Detectors

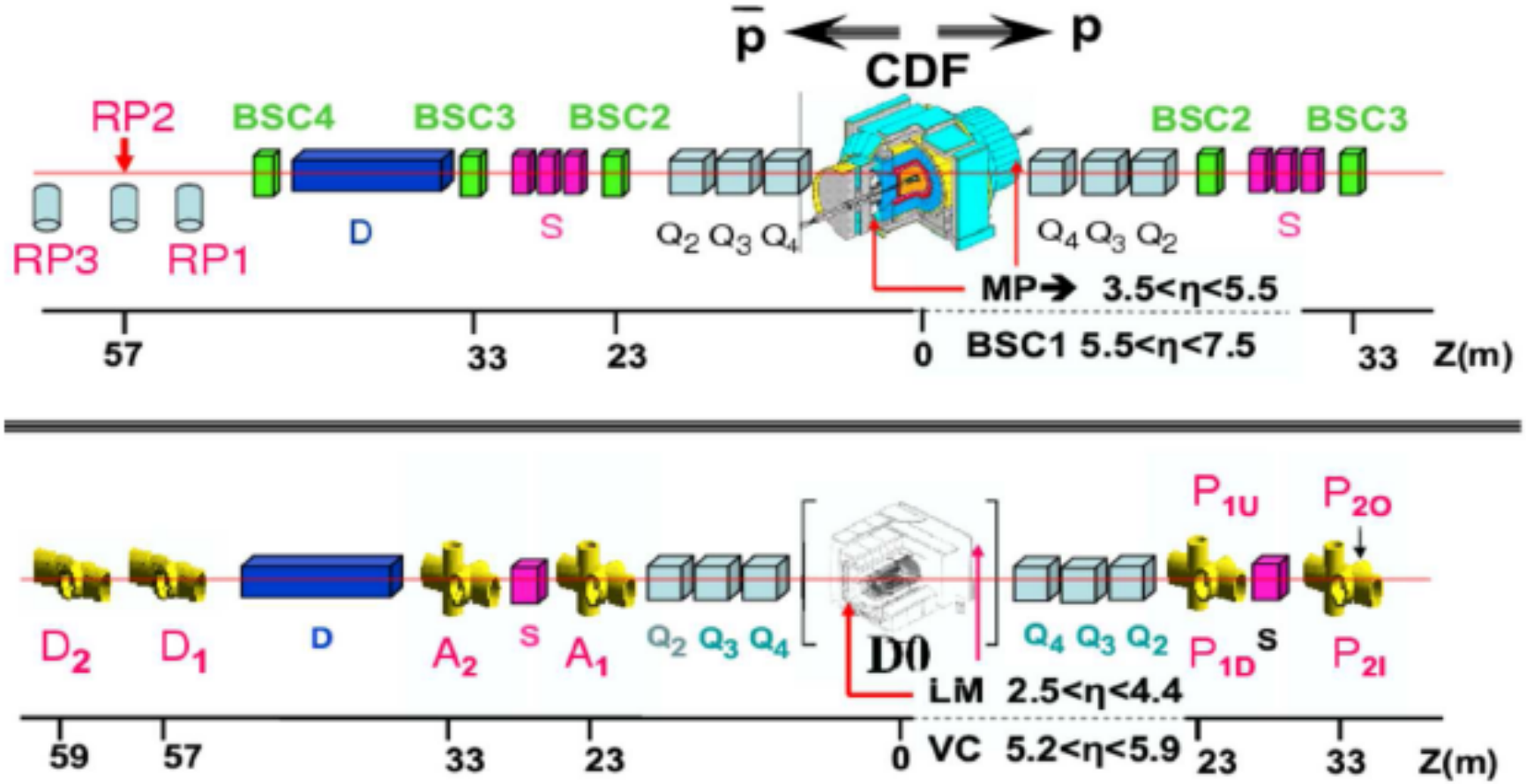
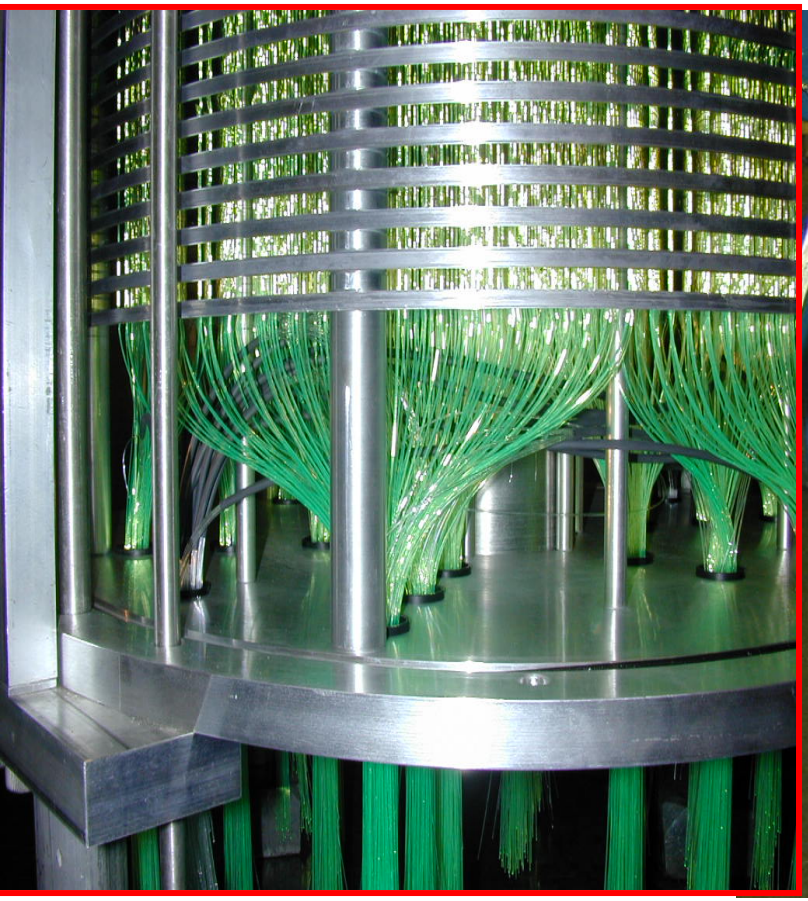


Figure 1: The CDF and D0 detectors in Run II

The MiniPlug Calorimeters

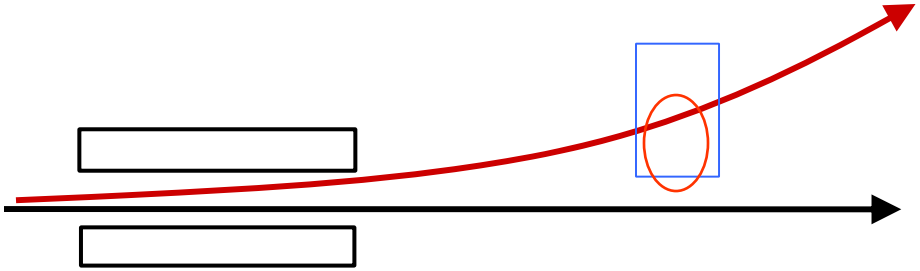




About 1500 wavelength shifting fibers of 1 mm dia. are 'strung' through holes drilled in 36x$\frac{1}{4}$" lead plates sandwiched between reflective Al sheets and guided into bunches to be viewed individually by multi-channel photomultipliers.

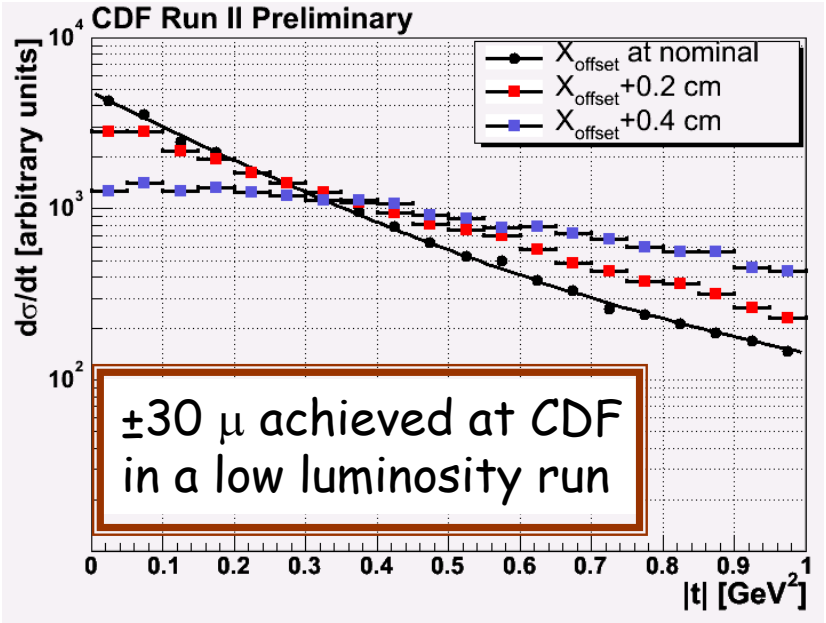
Alignment of RPS using Data

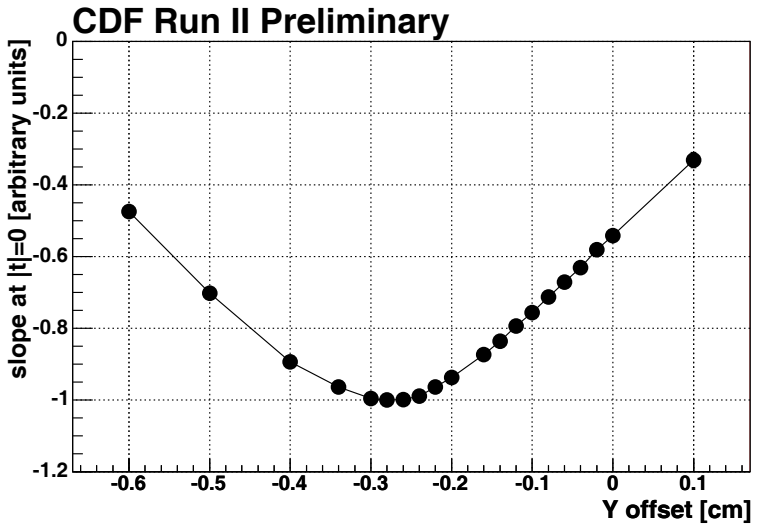
Proposed for the FP420 project at the LHC

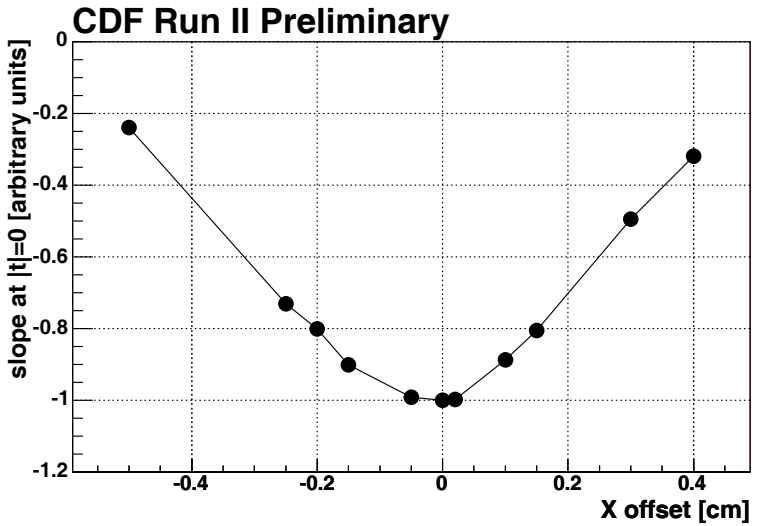


maximize the |t|-slope

⇨ determine X and Y offsets







Diffraction at CMS

What can we learn/expect *on elastic and diffractive scattering* from the LHC experiments ?

K. Goulianos

- contribution to the discussion session

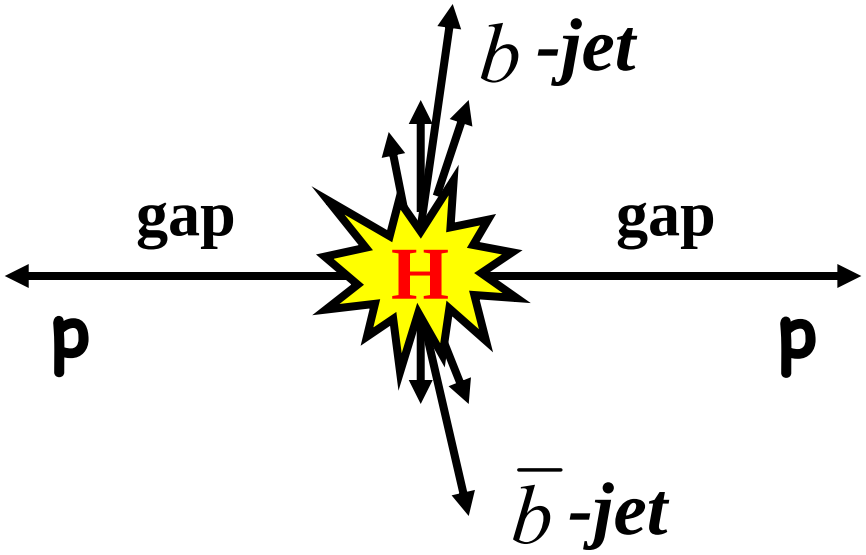


2 What to do at the LHC

goal	· understand the QCD basis of diffraction and discover new physics
exploit	· large $\sqrt{s} \Rightarrow$ large σ, $\Delta\eta$, E_T
TEV2LHC	· from Tevatron to LHC: confirm, extend, discover...
	$\Rightarrow$ confirm Tevatron results and extend them into the new kinematic domain
specifics	· elastic diffractive, total cross sections, and ρ-value
	$\Rightarrow$ diffractive structure function: dijets vs. W-boson, ...
	$\Rightarrow$ multi-gap configurations
	$\Rightarrow$ jet·gap·jet: $d\sigma/d\Delta\eta$ vs. $E_T^{\rm jet} \Rightarrow$ BFKL, Mueller-Navelet jets

- FP420 project – forward proton at 420 - Joint CMS / ATLAS R&D project
- HPS project – high precision spectrometer - a CMS proposal

The engine of the diffractive program at LHC: EXCLUSIVE JJ & HIGGS BOSON PRODUCTION



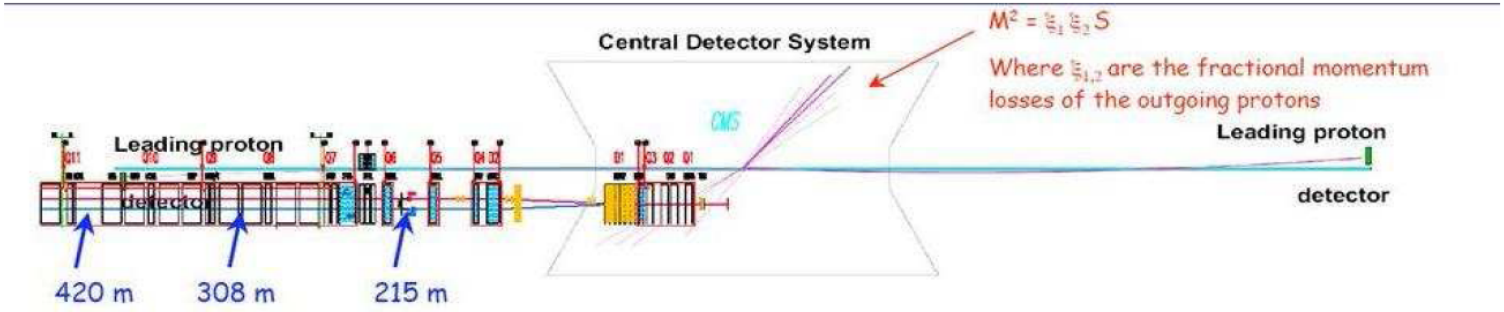
$M_H^2 = (p + \bar{p} - p' - \bar{p}')^2$ ➔ $\Delta M \sim (1\text{-}2)$ GeV

Determine spin of H

The FP420 Project

- **alignment:** study the use of our alignment method in FP420;
- **backgrounds:** study the backgrounds expected using our CDF experience;
- **physics:** explore physics aspects that may lead to discoveries.

An example of the latter is the measurement of the parton distribution density of the proton in the very low-x region accessible with the forward detectors.



TOTEM/CMS
ATLAS

FP420 project: http://www.fp420.com/
Measure protons at 420 m from the IP during normal high luminosity running to be used in conjunction with CMS and ATLAS
Feasibility study and R&D for Roman Pot detector development

- Physics aim :pp → p+ X + p (Higgs, New physics, QCD studies)
- Status: Completed Jun 2008: arXiv:0806.0302

The HPS Project

CMS Internal Note (CONFIDENTIAL) October 30th, 2009

High Precision Spectrometers – HPS Project

A staged installation is proposed starting with detectors at 240 m in 2010

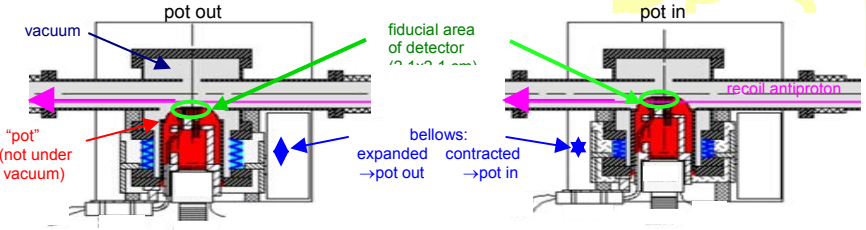
"Diffraction at CDF and Cross Sections at the LHC"
- Talk in preparation for the annual Manchester meeting Dec 2009

http://www.fp420.com/conference/dec2009/program.html

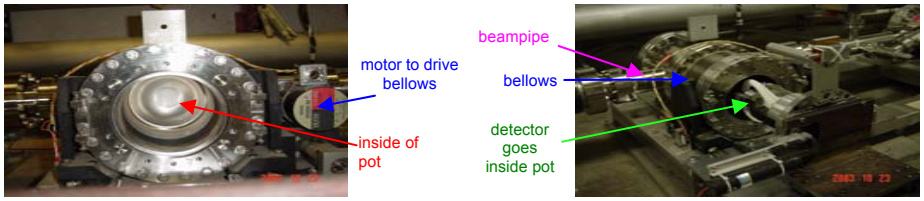


The Roman-Pot Detectors at CDF

Concept of a Roman Pot

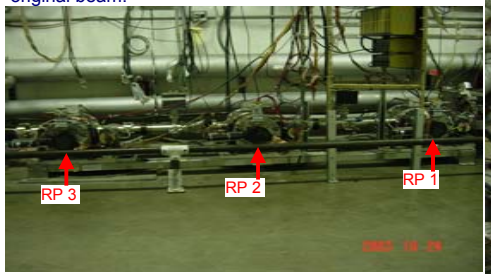


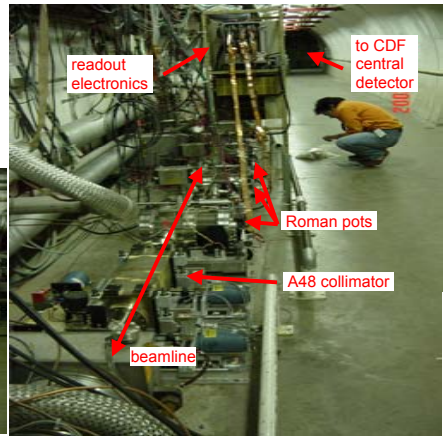
Bellows allow detectors to move close to the beam while maintaining vacuum



In the Tevatron Tunnel

CDF had three Roman pots (RP1, RP2, RP3) located 57m downstream of the interaction point along the antiproton beam direction.
They were used to detect antiprotons which underwent a "diffractive" interaction and were scattered in a direction very close to that of the original beam.

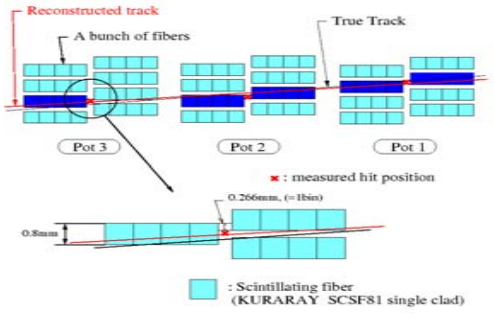




Roman-Pot Detector Design – by The Rockefeller University

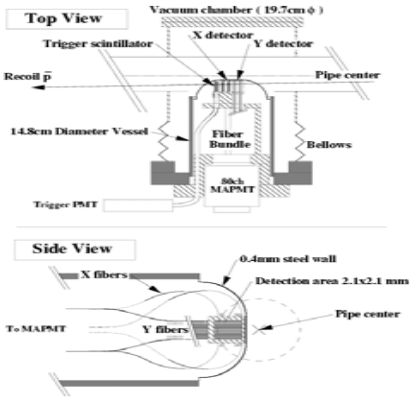
The three Roman pots each contain detectors consisting of:

- Trigger scintillation counter 2.1x2.1x0.8 cm^3
- 40 X + 40 Y fiber readout channels
  - Each consists of 4 (→ bigger signal) clad scintillating fibers 0.8x0.8 mm^2 (new technology at the time)
  - X,Y each have 2 rows of 20 fibers spaced 1/3 fiber width apart for improved position resolution (three times better than with a single row)



Expected position resolution	80 μm
Expected angle resolution	60 μrad

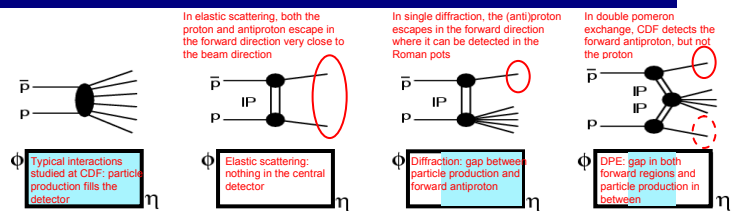
CDF "Tokyo"-Pot Detectors – Built by the University of Tsukuba, Japan





Physics Using the Roman-Pot Detectors

- The Roman-pot detectors are used to study diffractive interactions
- Elastic scattering was measured by CDF in 1988-1989 using Roman pots (not those described here) in both the proton and antiproton direction



Path of the Antiproton through the Tevatron Magnets

- Dipole magnets bend recoil antiprotons which have lost momentum towards the inside of the Tevatron ring, into the Roman pots
- Knowledge of the beam optics, the collision vertex position, and the antiproton track position and angle in the Roman-pot detectors are used to reconstruct the kinematics of the diffractive antiproton

